



Title	Ultrathin Cobalt-Manganese Nanosheets: An Efficient Platform for Enhanced Photoelectrochemical Water Oxidation with Electron-Donating Effect
Author(s)	Yang, Gaoliang; Li, Yunxiang; Pang, Hong; Chang, Kun; Ye, Jinhua
Citation	Advanced Functional Materials, 29(46), 1904622 <a href="https://doi.org/10.1002/adfm.201904622">https://doi.org/10.1002/adfm.201904622</a>
Issue Date	2019-11-14
Doc URL	<a href="http://hdl.handle.net/2115/79747">http://hdl.handle.net/2115/79747</a>
Rights	This is the peer reviewed version of the following article: Yang, G., Li, Y., Pang, H., Chang, K., Ye, J., Ultrathin Cobalt–Manganese Nanosheets: An Efficient Platform for Enhanced Photoelectrochemical Water Oxidation with Electron Donating Effect. Adv. Funct. Mater. 2019, 29, 1904622, which has been published in final form at <a href="https://doi.org/10.1002/adfm.201904622">https://doi.org/10.1002/adfm.201904622</a> . This article may be used for non-commercial purposes in accordance with Wiley Terms and Conditions for Use of Self-Archived Versions.
Type	article (author version)
File Information	manuscript.pdf



[Instructions for use](#)

**Ultrathin Cobalt-Manganese Nanosheets: An Efficient Platform for Enhanced Photoelectrochemical Water Oxidation with Electron-Donating Effect**

*Gaoliang Yang, Yunxiang Li, Hong Pang, Kun Chang, and Jinhua Ye\**

G. Yang, Y. Li, Dr. H. Pang, Prof. J. Ye

Graduate School of Chemical Science and Engineering, Hokkaido University, Sapporo 060-0814, Japan

E-mail: Jinhua.YE@nims.go.jp

G. Yang, Y. Li, Dr. H. Pang, Prof. J. Ye

International Center for Materials Nanoarchitectonics (WPI-MANA), National Institutes for Materials Science (NIMS), 1-1 Namiki, Tsukuba, Ibaraki 305-0044, Japan

Prof. J. Ye

TJU-NIMS International Collaboration Laboratory, School of Materials Science and Engineering, Tianjin University, Tianjin 300072, P. R. China

Prof. J. Ye

Collaborative Innovation Center of Chemical Science and Engineering (Tianjin), Tianjin 300072, P. R. China

Prof. K. Chang

College of Material Science and Engineering, Nanjing University of Aeronautics and Astronautics, Nanjing, 210016, P. R. China

**Keywords:** (Cobalt-manganese nanosheets, electron-donating effect, photoelectrocatalysis, water oxidation)

**Abstract:** An ultrathin cobalt-manganese (Co-Mn) nanosheet, consisting of amorphous  $\text{Co(OH)}_x$  layers and ultras-small  $\text{Mn}_3\text{O}_4$  nanocrystals, is designed as an efficient co-catalyst on  $\alpha\text{-Fe}_2\text{O}_3$  film for photoelectrochemical (PEC) water oxidation. The uniformly distributed Co-Mn nanosheets lead to a remarkable 2.6-fold enhancement on the photocurrent density at 1.23 V vs. reversible hydrogen electrode (RHE) and an impressive cathodic shift ( $\sim 200$  mV) of onset potential compared with bare  $\alpha\text{-Fe}_2\text{O}_3$  film. Furthermore, the decorated photoanode exhibits a prominent resistance against photo-corrosion with an excellent stability for over 10 h. Detailed mechanism investigation manifests that incorporation of Mn sites in the nanosheets could create electron donation to Co sites and facilitate the activation of OH group, which drastically increases the catalytic activities for water oxidation. These findings provide valuable guidance for designing high-performance co-catalysts for PEC applications and open new avenues towards controlled fabrication of mixed metallic composites.

## 1. Introduction

Photoelectrochemical (PEC) water splitting is a promising approach providing a sustainable and environmental route for direct conversion of solar energy to hydrogen, which has been considered to play a vital role in coping with energy shortage and environmental pollution.<sup>[1-3]</sup> Because of the sluggish kinetics of four-electron processes for oxygen evolution reaction (OER), construction of efficient photoanodes is significantly challenging for solar-driven PEC water splitting.<sup>[4, 5]</sup>  $\alpha$ -Fe<sub>2</sub>O<sub>3</sub> is one of the most promising photoanode materials due to its abundance, nontoxicity, superior stability, and moderate bandgap (~ 2.1 eV). However, the performance of  $\alpha$ -Fe<sub>2</sub>O<sub>3</sub> is significantly restricted by its intrinsically poor conductivity, short hole diffusion length (2 ~ 4 nm) and limited photo-carrier lifetime.<sup>[6, 7]</sup> Thus, great efforts have been devoted to promoting those properties of  $\alpha$ -Fe<sub>2</sub>O<sub>3</sub> films, such as morphology controlling,<sup>[8-10]</sup> element doping<sup>[11-13]</sup> and heterojunction construction.<sup>[14-16]</sup> These strategies are expected to shorten the migration distance of charge carriers to the catalytic sites and reduce charge recombination in the bulk of  $\alpha$ -Fe<sub>2</sub>O<sub>3</sub> films. In this case, more photo-generated holes will be able to migrate to the catalytic surface. Afterwards, these holes will inject into the electrolyte and eventually participate in the reaction. However, the hole injection process proceeds along with serious surface recombination due to the presence of surface trapped sites and complicated OER mechanism.<sup>[17]</sup> Therefore, enhancing the surface hole injection efficiency should be strived for to rule over the PEC water oxidation process.

Notably, loading oxygen evolution catalysts (OECs) has been regarded as a particularly effective approach to enhance the surface reaction kinetics of  $\alpha$ -Fe<sub>2</sub>O<sub>3</sub> films.<sup>[18-20]</sup> The introduction of OECs is mainly meant to provide surface reaction sites with lower overpotentials for holes transfer at the interface of photoelectrode/electrolyte. In addition, OECs can also act as selective trapping sites for photogenerated electrons/holes, thus suppressing the surface charge recombination.<sup>[21, 22]</sup> The employed OECs in PEC system usually originate from superior electrocatalysts, among which lots of transition metal-based OECs with low cost have

been proved to have the ability of achieving low overpotentials for electrochemical OER.<sup>[23]</sup> Because of complicated processes and intermediates involved in OER, it is usually difficult for any single metal-based OECs to achieve comprehensive enhancement for PEC water splitting. Therefore, it is believed that bimetallic compounds, which are adjustable with different metal sites, are promising OECs for PEC water oxidation owing to their abundant active sites and versatility in composition.<sup>[17, 24-27]</sup> In this regard, it is significantly important to investigate the actual functions of different metal sites in the compounds and obtain deep understanding on the explicit mechanism of this type of OECs for PEC water oxidation. By this way, it is possible to open new avenue and provide guidance for designing high-efficiency OECs with multi-metallic sites for PEC water splitting.

Herein, a delicate OEC/ $\alpha$ -Fe<sub>2</sub>O<sub>3</sub> architecture is constructed through uniform decoration of ultrathin Co-Mn nanosheets. It was discovered that incorporation of Mn site in the nanosheets could create electron donation to Co site and facilitate the activation of OH group, which drastically boosted the intrinsic catalytic activities for PEC water oxidation. As a result, the optimized photoanode exhibited an excellent photocurrent density of 2.09 mA cm<sup>-2</sup> at 1.23 V vs. RHE under AM 1.5 G illumination (twice that of bare  $\alpha$ -Fe<sub>2</sub>O<sub>3</sub>), as well as remarkable stability for over 10 h. The Co-Mn nanosheets could also tune the charge behaviors with significantly enhanced surface charge transfer efficiency and charge separation efficiency. Furthermore, this deposition method could also be applied in composites with other metals, which is believed to be a versatile and promising strategy to decorate photoanode with various metallic composites. These findings also provide an insight into the activation of PEC water oxidation through electron withdrawing/donating induced by bimetallic site in the composites.

## 2. Results and Discussion

The synthetic approach of  $\alpha$ -Fe<sub>2</sub>O<sub>3</sub> films and fabrication processes of Co-Mn nanosheets are depicted in Figure 1(a). Firstly, a yellow layer of FeOOH nanorods (Figure 1b) was fabricated on a conducting glass substrate using a hydrothermal method. The FeOOH transformed to  $\alpha$ -

Fe<sub>2</sub>O<sub>3</sub> via calcination process with film's color changing from yellow to red. Then, Co-Mn nanosheets were deposited on the surface of  $\alpha$ -Fe<sub>2</sub>O<sub>3</sub> (Co-Mn- $\alpha$ -Fe<sub>2</sub>O<sub>3</sub>) with a facile and quick electrodeposition method. The optimized electrodeposition time is 30 s and Co/Mn ratio in the precursor solution is 0.5 : 0.5 (confirmed by morphology and photocurrent densities in Figure S5~S8; the corresponding discussion can be found in Supporting Information). Hereafter, all the characterizations and discussion of Co-Mn- $\alpha$ -Fe<sub>2</sub>O<sub>3</sub> films are based on these two optimized parameters, unless stated otherwise.

The XRD patterns of  $\alpha$ -Fe<sub>2</sub>O<sub>3</sub> and Co-Mn- $\alpha$ -Fe<sub>2</sub>O<sub>3</sub> films in Figure S1a display similar diffraction peaks ascribed to  $\alpha$ -Fe<sub>2</sub>O<sub>3</sub> and SnO<sub>2</sub> (from FTO substrate). It is notable that only distinct peaks of  $\alpha$ -Fe<sub>2</sub>O<sub>3</sub> at 35.6° and 63.9° could be observed (well indexed to the  $\alpha$ -Fe<sub>2</sub>O<sub>3</sub> crystal structure of PDF # 33-0664), presumably owing to its relatively small size and low loading amount compared with the SnO<sub>2</sub>. There is no peak ascribed to Co-Mn nanosheets in XRD results, which may be too thin to be detected. Figure S1b shows UV-vis spectra of  $\alpha$ -Fe<sub>2</sub>O<sub>3</sub> and Co-Mn- $\alpha$ -Fe<sub>2</sub>O<sub>3</sub> films. Bare  $\alpha$ -Fe<sub>2</sub>O<sub>3</sub> exhibits a light absorption edge of ~ 580 nm with a band gap energy of 2.09 eV (Tauc plots in Figure S2), which conforms well with the reported values.<sup>[28]</sup> After being decorated with Co-Mn nanosheets, the absorption intensity and bandgap remain almost unchanged, indicating ultrathin Co-Mn nanosheets have negligible influence on light adsorption of  $\alpha$ -Fe<sub>2</sub>O<sub>3</sub>. Therefore, XRD and UV-vis results manifest that the structure and optical absorption of  $\alpha$ -Fe<sub>2</sub>O<sub>3</sub> film would not be affected by the decoration of Co-Mn nanosheets.

The obtained  $\alpha$ -Fe<sub>2</sub>O<sub>3</sub> film displays a one-dimensional wormlike structure of nanorods array (Figure 1c). The thickness of the film is approximately 370 nm as identified by cross-section SEM image (Figure S3). Compared with pure  $\alpha$ -Fe<sub>2</sub>O<sub>3</sub> film, an ultrathin layer is fully covered on the surface of  $\alpha$ -Fe<sub>2</sub>O<sub>3</sub> after integration of Co-Mn nanosheets (images with larger magnification are presented in Figure S4). TEM image in Figure 2a further confirms that Co-Mn nanosheets are compactly coated on well crystalized  $\alpha$ -Fe<sub>2</sub>O<sub>3</sub> nanorods and the layer

thickness is only several nanometers. High-resolution TEM (HRTEM) images show that deposited Co-Mn nanosheets consist of amorphous layers and ultrasmall nanocrystals (Figure 2b). According to Yan's results with similar method, the amorphous layers are  $\text{Co(OH)}_x$  and the ultrasmall nanocrystals are  $\text{Mn}_3\text{O}_4$ , which are verified by the Raman and XRD measurements in Figure S10~S12.<sup>[29]</sup> The nanocrystalline  $\text{Mn}_3\text{O}_4$  are embedded in the  $\text{Co(OH)}_x$  matrix by forming solid interparticle contact between these two phases (confirmed by the AFM image in Figure S9), which can be described as a kind of mosaic structure. The lattice fringes with spacing of 0.204, 0.248 and 0.309 nm correspond to (220), (211) and (112) crystal planes, unveiling again that the nanocrystals are tetragonal  $\text{Mn}_3\text{O}_4$ .<sup>[30]</sup> EDS elemental mapping images illustrate that Co and Mn elements are relatively uniformly distributed along with Fe and O elements (Figure 2c~2g), further verifying the homogeneous coating of Co-Mn nanosheets on the surface of  $\alpha\text{-Fe}_2\text{O}_3$ .

The chemical states and elemental composition of Co-Mn- $\alpha\text{-Fe}_2\text{O}_3$  film were further characterized by X-ray photoelectron spectroscopy (XPS). The high resolution XPS spectrum of Fe 2p (Figure S13a) is composed of two major peaks located at 710.5 eV and 724.1 eV (corresponding to Fe 2p<sub>1/2</sub> and Fe 2p<sub>3/2</sub>), as well as a satellite peak (denoted as "Sat") at 718.5 eV, which confirms the existence of  $\text{Fe}^{3+}$ .<sup>[31]</sup> Additionally, the Fe 2p peaks are shifted to lower binding energy after the coating of Co-Mn nanosheets (Figure 3a), revealing that electrons can be transferred from Co-Mn nanosheets to  $\alpha\text{-Fe}_2\text{O}_3$ . This phenomenon confirms that Co-Mn nanosheets could facilitate charge transfer on the photoanode and thus reduce charge recombination. The O 1s spectrum (Figure S13b) can be fitted into two peaks, which are assigned to the lattice oxygen (O<sub>L</sub>) and hydroxyl groups bonded with metal cations (O<sub>H</sub>), respectively.<sup>[32]</sup> The Co 2p spectrum (Figure 3b) also shows two main peaks at around 780.2 eV and 796.1 eV (corresponding to Co 2p<sub>3/2</sub> and Co 2p<sub>1/2</sub>), with two shake-up satellite peaks (about 786.0 eV and 802.8 eV). The two main peaks can be deconvolved into four peaks, corresponding to Co (III) and Co (II).<sup>[17, 33]</sup> The fitting results indicate that the content of Co

(III) is relatively higher than Co (II) in the composite, which is favorable for the superior catalytic activity.<sup>[17]</sup> Additionally, satellite peak located at 786.0 eV can be attributed to the Co-hydroxyl groups, which is consistent with the XPS result of O 1s at 531.3 eV.<sup>[34]</sup> The formation of Co-hydroxyl groups would yield positive effects on the OER performance, since it might induce structural flexibility along with optimized coordination states.<sup>[35]</sup> Similarly, the Mn 2p spectrum (Figure 3c) is also composed of two main peaks (could be fitted to Mn (II) and Mn (III), respectively), which is consistent with the TEM results.<sup>[30]</sup> In order to investigate the electronic structure modulation between Co and Mn, the Co 2p spectra of Co-Mn- $\alpha$ -Fe<sub>2</sub>O<sub>3</sub> and Co- $\alpha$ -Fe<sub>2</sub>O<sub>3</sub> are compared in Figure 3d. The composition and configuration of these two spectra are similar. However, an obvious negative shift (0.57 eV) can be observed, indicating the electron donation from Mn site to Co site. This strong electronic interaction between Co and Mn would make Co site more readily to accept holes, which might facilitate the generation of intermediates and hence accelerate the O<sub>2</sub> production. The electron donation would also induce Mn<sub>3</sub>O<sub>4</sub> to become more Lewis acidic, whereby the activation of OH group through Lewis acid-base interaction could occur.<sup>[36]</sup>

The PEC performance of different photoanodes were evaluated by measuring the photocurrent density versus applied potential ( $J$ - $V$ ) curves under AM 1.5 G irradiation. As displayed in Figure 4a, a photocurrent density of 2.09 mA cm<sup>-2</sup> at 1.23 V vs. RHE is achieved for Co-Mn- $\alpha$ -Fe<sub>2</sub>O<sub>3</sub> photoanode, about 1.6 times higher than that of bare  $\alpha$ -Fe<sub>2</sub>O<sub>3</sub> photoanode (0.83 mA cm<sup>-2</sup>). In addition, the onset potential shows a great cathodic shift compared with pristine  $\alpha$ -Fe<sub>2</sub>O<sub>3</sub> photoanode, indicating a lower overpotential for water oxidation as a result of decoration of Co-Mn nanosheets. The enhanced photocurrent density and lower onset potential of Co-Mn- $\alpha$ -Fe<sub>2</sub>O<sub>3</sub> photoanode could be attributed to the compact contact between ultrathin Co-Mn nanosheets and oriented  $\alpha$ -Fe<sub>2</sub>O<sub>3</sub> nanorods. Such intimate interaction was expected to facilitate the charge separation at the photoelectrode/electrolyte interface, which would promote the oxygen evolution kinetics of the photoanode.<sup>[25]</sup> Additionally, the photocurrent density at

1.23 V vs. RHE of Co-Mn- $\alpha$ -Fe<sub>2</sub>O<sub>3</sub> photoanode is also much higher than Mn- $\alpha$ -Fe<sub>2</sub>O<sub>3</sub> (1.17 mA cm<sup>-2</sup>), Co- $\alpha$ -Fe<sub>2</sub>O<sub>3</sub> (1.56 mA cm<sup>-2</sup>) and other photoanodes with different Co/Mn ratios (Figure S8) under the same condition. This phenomenon elucidates that OECs with single element can hardly realize the acceleration of all processes for PEC water oxidation simultaneously. Moreover, suitable Co/Mn ratio is significantly important to achieve remarkable performance for the reaction.

In order to explain the importance of appropriate Co/Mn ratio and further illustrate the electron-withdrawing/donating effect between Co and Mn sites, Co 2p spectra of Co<sub>0.75</sub>-Mn<sub>0.25</sub>- $\alpha$ -Fe<sub>2</sub>O<sub>3</sub> (the ratio of Co and Mn in precursor solution is 0.75:0.25) and Co<sub>0.25</sub>-Mn<sub>0.75</sub>- $\alpha$ -Fe<sub>2</sub>O<sub>3</sub> (the ratio of Co and Mn in precursor solution is 0.25:0.75) are compared with Co- $\alpha$ -Fe<sub>2</sub>O<sub>3</sub> (Figure S14). Similar with the result of Co-Mn- $\alpha$ -Fe<sub>2</sub>O<sub>3</sub>, obvious negative shifts of 0.32 eV and 0.74 eV can be observed for Co<sub>0.75</sub>-Mn<sub>0.25</sub>- $\alpha$ -Fe<sub>2</sub>O<sub>3</sub> and Co<sub>0.25</sub>-Mn<sub>0.75</sub>- $\alpha$ -Fe<sub>2</sub>O<sub>3</sub>, respectively. The shift of Co 2p spectra becomes larger with the increasing of Mn ratio, verifying the stronger electron-donating effect from Mn site to Co site. However, the Co<sub>0.25</sub>-Mn<sub>0.75</sub>- $\alpha$ -Fe<sub>2</sub>O<sub>3</sub> only showed moderate photocurrent density although with the strongest interaction between Co and Mn sites. The presumed reason could be attributed to the low concentration of Co, suggesting that the active sites might be not enough. The XPS results of Co<sub>0.75</sub>-Mn<sub>0.25</sub>- $\alpha$ -Fe<sub>2</sub>O<sub>3</sub> and Co<sub>0.25</sub>-Mn<sub>0.75</sub>- $\alpha$ -Fe<sub>2</sub>O<sub>3</sub>, combined with the results in Figure 3d, unravel the importance of electron-donating effect for the activity. Generally, the formation of the absorbed OOH species during OER is considered as the rate limiting step for further processes.<sup>[37]</sup> Furthermore, the interaction between absorbed OOH species and 3d orbital of transition metal sites determines the OER activities of transition metal-based catalysts.<sup>[24, 38]</sup> In this regard, the Mn sites would lower the energy of Co atoms and enable the Co sites to gain more electrons, thus inducing the electron-donating effect. The increase of electron density in 3d orbital of Co sites was previously reported to favor the generation of absorbed OOH species, which is beneficial for facilitating the OER processes.<sup>[39, 40]</sup>

The photoconversion efficiencies of different photoanodes were evaluated by the applied bias photon-to-current conversion efficiency (ABPE), calculated from the  $J-V$  curves. As shown in Figure 4b, the ABPE of  $\alpha$ -Fe<sub>2</sub>O<sub>3</sub> photoanode presents a peak of only 0.08% at 1.04 V vs. RHE, while the ABPE peaks of Mn- $\alpha$ -Fe<sub>2</sub>O<sub>3</sub> and Co- $\alpha$ -Fe<sub>2</sub>O<sub>3</sub> photoanodes reach 0.12% (at 1.02 V vs. RHE) and 0.19% (at 0.99 V vs. RHE), respectively. In contrast, Co-Mn nanosheets can further promote the maximum ABPE to as high as 0.25% at a lower potential of 0.98V vs. RHE, which is nearly threefold higher than that of bare  $\alpha$ -Fe<sub>2</sub>O<sub>3</sub> photoanode.

In order to further verify the catalytic effect of Co-Mn nanosheets, the incident photo-to-electron conversion efficiency (IPCE) spectra are displayed as a function of wavelength from 360 to 600 nm in Figure 4c. An obvious enhancement can be observed at the whole range of spectrum after modification with the OECs. It is demonstrated that Co-Mn- $\alpha$ -Fe<sub>2</sub>O<sub>3</sub> photoanode achieves the maximum IPCE value of 39.1% at 360 nm, about 3.7 times higher than that of bare  $\alpha$ -Fe<sub>2</sub>O<sub>3</sub> photoanode (10.6% at 360 nm). The enhanced IPCE of Co-Mn- $\alpha$ -Fe<sub>2</sub>O<sub>3</sub> photoanode is also consistent with the result of  $J-V$  curves, both of which are comparable with recent reported results of  $\alpha$ -Fe<sub>2</sub>O<sub>3</sub> based photoanodes coupled with different OECs (Table S3). Notably, the trends of IPCE with wavelengths for all photoanodes are similar (with an onset wavelength of about 600 nm, which are also in accordance with the UV-vis spectra), but the IPCE values exhibit significant improvement after decoration with Co-Mn nanosheets. Considering the same semiconductor properties of  $\alpha$ -Fe<sub>2</sub>O<sub>3</sub>, the only difference between these photoanodes is the decoration of different OECs. Accordingly, the enhanced performance is not related to the light absorption, but reduced electron trapping sites at the surface and better charge carrier extraction efficiency by the formation of interface between Co-Mn nanosheets and  $\alpha$ -Fe<sub>2</sub>O<sub>3</sub> nanorods (will be discussed in more detail later).<sup>[41]</sup>

To examine the photo-response of different photoanodes over time, current-time curves were measured at 1.23 V vs. RHE under chopped illumination (Figure 4d). The Co-Mn- $\alpha$ -Fe<sub>2</sub>O<sub>3</sub> photoanode showed a quick and steady current response, with a highest stable photocurrent

density of  $2.07 \text{ mA cm}^{-2}$ , which is nearly same as the  $J-V$  curve data. It is notable that bare  $\alpha\text{-Fe}_2\text{O}_3$  photoanode presented a small spike once the light was turned on. This phenomenon might be attributed to the slow OER kinetics compared with the rapid hole consumption to the surface trapping states, inducing an electron flux associated with recombination. To obtain steady photocurrents, the prevalent strategy is to eliminate those surface trapping sites for holes accumulation by introducing a passivation layer.<sup>[42-44]</sup> After being decorated with Co-Mn nanosheets, a uniform layer could be formed on the surface of  $\alpha\text{-Fe}_2\text{O}_3$  nanorods. In this case, the photoanode exhibited quick current response to the chopped light and the photocurrent could be reproduced via several cycles, which could be ascribed to the enhanced charge utilization efficiency and passivated surface trapping sites.

To understand the underlying mechanism of Co-Mn nanosheets for enhancing PEC performance of  $\alpha\text{-Fe}_2\text{O}_3$  films, charge transfer behaviors of the photoanodes were investigated by electrochemical measurements. Due to the low activation energy and kinetically facile photo-oxidation of  $\text{SO}_3^{2-}$  species,  $J-V$  curves of the photoanodes were measured with  $\text{Na}_2\text{SO}_3$  as hole scavenger (Figure S15).<sup>[28]</sup> Then, the surface charge injection efficiency ( $\eta_{\text{inj}}$ ) and charge separation efficiency ( $\eta_{\text{sep}}$ ) were calculated according to the equations in experimental section. As shown in Figure 5a and Figure 5b, the  $\eta_{\text{inj}}$  and  $\eta_{\text{sep}}$  values of Co-Mn- $\alpha\text{-Fe}_2\text{O}_3$  photoanode are both much higher than that of pure  $\alpha\text{-Fe}_2\text{O}_3$  photoanode, while Mn- $\alpha\text{-Fe}_2\text{O}_3$  and Co- $\alpha\text{-Fe}_2\text{O}_3$  photoanodes only exhibit moderate values. These results are consistent with the PEC performance test, demonstrating that the positive outcomes could not only be ascribed to the improved water oxidation kinetics, but also the reduced surface charge recombination due to the electron-donating effect within Co-Mn nanosheets.

To gain more insight into the impacts of Co-Mn nanosheets modification to charge transfer and separation processes, Mott-Schottky analysis was conducted (Figure 5c). It is clearly presented that all photoanodes exhibit positive slopes, manifesting n-type semiconductor feature. The flat-band potentials display a gradually cathodic shift from bare  $\alpha\text{-Fe}_2\text{O}_3$  to Co-

Mn- $\alpha$ -Fe<sub>2</sub>O<sub>3</sub> photoanode and the slopes of Mott–Schottky curves show an evident decrease after OECs loading. The values of carrier density ( $N_d$ ), which derives from the slope of Mott–Schottky curves, promote from  $1.34 \times 10^{20} \text{ cm}^{-3}$  to  $5.41 \times 10^{20} \text{ cm}^{-3}$  (Table S1). The enhancement of  $N_d$  could promote band bending at the interface of electrode/electrolyte, facilitating the processes of charge transfer.<sup>[45]</sup> In this case, the results of Mott–Schottky analysis are consistent with PEC Na<sub>2</sub>SO<sub>3</sub> oxidation test, verifying more effective processes of charge separation and holes injection with decoration of Co-Mn nanosheets.

To visualize the charge transfer processes at the interface of electrode/electrolyte, electrochemical impedance spectroscopy (EIS) was measured at 1.23 V vs. RHE under illumination. As demonstrated in Figure 5d, all the Nyquist plots of four photoanodes show two obvious semicircles. The small semicircle in high-frequency range is usually regarded as charge transfer process in the bulk of semiconductor, while the large semicircle of low-frequency region is deemed as charge transfer behavior at electrode/electrolyte interface. Both of the semicircles are smaller for the OECs loaded photoanodes, indicating a faster surface water oxidation process benefited by efficient hole extraction and oxidization catalytic capability.<sup>[46]</sup> In order to investigate the EIS data more thoroughly, a typical equivalent circuit model inserted in Figure 5d is proposed and the fitted results are presented with solid lines. In this case,  $R_s$  indicates the series resistance, representing the resistivity of electrolyte between working and reference electrodes,  $R_{\text{bulk}}$  in high frequency represents resistance in the semiconductor,  $R_{\text{ct}}$  in low frequency defines as charge transfer resistance across the interface of photoanode/electrolyte and CPE is the constant phase element.<sup>[28, 46]</sup> The values of all these items are displayed in Table S2, in which  $R_s$  for all photoanodes are almost same, suggesting similar working condition of these photoanodes. Furthermore, the values of  $R_{\text{bulk}}$  for photoanodes of Mn- $\alpha$ -Fe<sub>2</sub>O<sub>3</sub> (60.77  $\Omega$ ), Co- $\alpha$ -Fe<sub>2</sub>O<sub>3</sub> (38.41  $\Omega$ ) and Co-Mn- $\alpha$ -Fe<sub>2</sub>O<sub>3</sub> (28.19  $\Omega$ ) are all lower than that of pristine  $\alpha$ -Fe<sub>2</sub>O<sub>3</sub> (103.7  $\Omega$ ), demonstrating enhanced conductivity ascribing to the incorporation of OECs. The improved charge transfer in the bulk might be

attributed to the facilitated charge separation, indicating the OECs have additional effects on promoting the PEC water oxidation in addition to the surface catalytic effect.<sup>[17]</sup> A significant decrease can be observed in  $R_{ct}$  from 564.9  $\Omega$  to 299.7  $\Omega$  after the decoration of Co-Mn nanosheets, proposing that the photogenerated charge carriers could be injected into electrolyte more easily on Co-Mn- $\alpha$ -Fe<sub>2</sub>O<sub>3</sub> photoanode.

Long-term stability test was carried out at 1.23 V vs. RHE under AM 1.5 G illumination to probe the durability of the photoelectrodes under constant working condition. As shown in Figure S17, Co-Mn- $\alpha$ -Fe<sub>2</sub>O<sub>3</sub> photoanode demonstrates an impressive stability over 10 h consecutive illumination, still retaining approximately 97 % of the initial photocurrent density. The H<sub>2</sub> on the Pt electrode and the O<sub>2</sub> on the Co-Mn- $\alpha$ -Fe<sub>2</sub>O<sub>3</sub> photoanode are 363.6 and 179.6  $\mu\text{mol cm}^{-2}$  after 10 h of consecutive light illumination, respectively, corresponding to the  $\approx 2:1$  ratio of the water splitting reaction (Figure S18). In addition, a high Faradaic efficiency of 95.8% is calculated based on the amount of the generated oxygen and the holes, indicating that nearly all the photogenerated holes are used for water oxidation. Furthermore, SEM images of Co-Mn- $\alpha$ -Fe<sub>2</sub>O<sub>3</sub> photoanode after stability test confirm that the morphology of Co-Mn nanosheets is maintained (Figure S19), indicating that Co-Mn nanosheets are stable as OEC under photooxidation environment. Moreover, the fitting XPS result of Co 2p for Co-Mn- $\alpha$ -Fe<sub>2</sub>O<sub>3</sub> photoanode after OER shows that the main peaks are similar compared to the result before OER (Figure S20), with only slightly increased content of Co (III) after stability test. The results after stability test further highlight the pivotal role of Co-Mn nanosheets in preventing photo-corrosion and prompting PEC performance of photoanode. Since Co-Mn nanosheets could achieve superior OER activity, we further investigated whether other composites (such as Ni-Mn composite and Fe-Mn composite) had similar enhancement effects on  $\alpha$ -Fe<sub>2</sub>O<sub>3</sub>. As shown in Figure S21, the morphologies of Ni-Mn- $\alpha$ -Fe<sub>2</sub>O<sub>3</sub> and Fe-Mn- $\alpha$ -Fe<sub>2</sub>O<sub>3</sub> are similar with Co-Mn- $\alpha$ -Fe<sub>2</sub>O<sub>3</sub>, with a thin layer coating on the surface of  $\alpha$ -Fe<sub>2</sub>O<sub>3</sub> nanorods.  $J$ - $V$  curves presented in Figure S22 demonstrate that Ni-Mn composite and Fe-Mn composite

could also enhance the OER performance of  $\alpha$ -Fe<sub>2</sub>O<sub>3</sub> films, suggesting the versatility of our strategy.

Based on above discussion, the proposed electron transfer paths for Co-Mn- $\alpha$ -Fe<sub>2</sub>O<sub>3</sub> photoanode are schematically illustrated in Figure 6. Under illumination,  $\alpha$ -Fe<sub>2</sub>O<sub>3</sub> can generate electrons and holes. Then the photo-generated electrons will migrate to FTO substrate, while the holes transfer to the surface driven by electric field. The surface-reaching holes are inclined to accumulate and recombine with the electrons due to sluggish kinetics of water oxidation and intrinsic properties of  $\alpha$ -Fe<sub>2</sub>O<sub>3</sub>. However, with the modification of Co-Mn nanosheets, photo-generated holes will migrate to the OEC layer and the recombination of charge carriers will be restricted. Co ions act as active sites to receive holes from semiconductor and then be oxidized to various high-value states.<sup>[47]</sup> The oxidation state of Co ions with high values (Co<sup>3+</sup> or Co<sup>4+</sup>) will then deliver the positive charge to the coordinated intermediate species to generate O<sub>2</sub> and recover to the initial states.<sup>[48]</sup> The electrons can migrate from Mn site to Co site via the intimate interface, indicating that chemical states of Co will become lower (the Co<sup>2+</sup> and Co<sup>3+</sup> will be changed to Co<sup>2- $\sigma$</sup>  and Co<sup>3- $\sigma$</sup> ). Consequently, the active sites of Co are inclined to accept the holes more easily, which is consistent with the high surface charge injection efficiency. The greater number of electrons in Co sites could also facilitate the generation of absorbed OOH intermediates and thus accelerate the O<sub>2</sub> production.<sup>[40, 49]</sup>

### 3. Conclusion

In conclusion, we have constructed ultrathin Co-Mn nanosheets as OEC for  $\alpha$ -Fe<sub>2</sub>O<sub>3</sub> films and investigated the electron-withdrawing/donating effect between Co(OH)<sub>x</sub> and Mn<sub>3</sub>O<sub>4</sub> to enhance the activity of photoanodes for PEC water oxidation. This approach helps in attaining an advantageous OEC/semiconductor interface to reduce recombination of photogenerated charge carriers and enhance their transfer efficiency. Compared with bare  $\alpha$ -Fe<sub>2</sub>O<sub>3</sub> photoanode, the optimized photoanode exhibits a remarkable photocurrent density of 2.09 mA cm<sup>-2</sup> at 1.23 V vs. RHE under AM 1.5 G illumination and an impressive cathodic shift (~ 200 mV) of onset

potential. Furthermore, Co-Mn nanosheets can also significantly enhance the ABPE values of  $\alpha$ -Fe<sub>2</sub>O<sub>3</sub> even at a lower potential and provide a remarkable resistance against photo-corrosion with an excellent stability for over 10 h. Detailed mechanism investigation unveils the pivotal role of electron-donation effect from Mn<sub>3</sub>O<sub>4</sub> to Co(OH)<sub>x</sub> resulting in efficient charge injection processes and thus dramatically enhanced PEC water oxidation performance. Our work provides deep understanding on the electron-withdrawing/donating effect for catalytic materials with multi-metallic sites, which possesses huge potentials in solving the current dilemma for large-scale applications of PEC water splitting.

#### 4. Experimental Section

*Preparation of  $\alpha$ -Fe<sub>2</sub>O<sub>3</sub> films:*  $\alpha$ -Fe<sub>2</sub>O<sub>3</sub> films were prepared according to the previous report.<sup>[11]</sup> Briefly, 0.15 M of FeCl<sub>3</sub> and 1 M NaNO<sub>3</sub> were dissolved in 40 ml water with the pH adjusted to 1.50 by HCl. The aqueous solution was transferred to a Teflon-lined stainless steel autoclave. Then the fluorine-doped tin oxide (FTO) glasses, which were ultrasonically cleaned with ethanol, acetone and deionized water sequentially for 1h to remove the organic contamination and dust, were immersed and placed with the conductive side facing to the wall of the autoclave. The autoclave was then put into the oven and heated at 95 °C for 4 h. A uniform layer of FeOOH (yellow color) was deposited on the FTO glasses. The substrates were washed with deionized water to remove the residual FeOOH and subsequently calcinated at 550 °C for 2 h and 800 °C for additional 20 min.

*Deposition of Co-Mn nanosheets on the  $\alpha$ -Fe<sub>2</sub>O<sub>3</sub> films:* The Co-Mn nanosheets was electrodeposited from a 2 mM solution with Co(NO<sub>3</sub>)<sub>2</sub> and Mn(NO<sub>3</sub>)<sub>2</sub> by applying a cathodic current density of 1 mA cm<sup>-2</sup>. The deposition durations were varied to 15, 30, 60, 90 and 120s for obtaining the optimized deposition time and investigating the growth kinetics of Co-Mn nanosheets. In order to obtain the optimized ratio of Co and Mn, different Co/Mn ratios of deposited composites were investigated by varying the Co/Mn ratios in the precursor solution. After electrodeposition, the as-obtained samples were thoroughly cleaned with deionized water

for several times and dried at 40 °C for 6 h. Other hybrid materials such as Ni-Mn composite and Fe-Mn composite were prepared by the same procedure as that used for the synthesis of Co-Mn nanosheets except different metal precursors.

*Materials characterization:* In our investigation, X-ray diffraction (XRD) patterns were measured on an X-ray diffractometer (X'pert powder, PANalytical B.V.) with Copper-K $\alpha$  radiation under 40 kV and 30 mA. Optical absorption properties of the photoelectrodes were measured over an ultraviolet–visible (UV–vis) spectrophotometer (UV-2700, Shimadzu). The morphologies of the films were characterized by scanning electron microscopy (SEM) (S-4800, Hitachi) and transmission electron microscopy (TEM) (FEI Tecnai G2 F30), coupled with energy dispersive spectrometer (EDS) to determine elementary composition. X-ray photoelectron spectroscopy (XPS) (PHI Quantera SXM, ULVAC-PHI) experiments were performed in a Theta probe using monochromated Mg K $\alpha$  x-rays at  $h\nu = 1486.6$  eV. Peak positions were internally referenced to the C 1s peak at 284.6 eV.

*Photoelectrochemical (PEC) measurements:* The PEC characterization was carried out using three-electrode cell system, in which a piece of pure platinum and an Ag/AgCl (3 M KCl) electrode as counter and reference electrodes, respectively. 1M NaOH aqueous solution was used as electrolyte (pH=13.6). The available electrode area immersed in the electrolyte solution was fixed to  $1.0 \times 1.0$  cm<sup>2</sup>. AM 1.5 G solar simulation (WXS-80C-3 AM 1.5 G) with a light intensity of 100 mW cm<sup>-2</sup> was utilized as the light sources. Photocurrent–potential ( $J$ – $V$ ) curves were obtained using linear sweep voltammogram in a voltage window of 0.6 ~ 1.6 V vs. RHE with a scan rate of 20 mV s<sup>-1</sup> on an electrochemical workstation (ALS/CH model 650A) and the light was chopped manually at regular intervals. Electrochemical impedance spectroscopy (EIS) test was performed at a DC bias of 1.23 V vs. RHE under AM 1.5 G illumination (frequency range: 0.1 ~ 100000 Hz). Mott–Schottky curves were obtained from 0.2 to 1.0 V vs. RHE in the dark at a frequency of 1000 Hz. All the potentials in the PEC performance vs. Ag/AgCl could be converted to the RHE scale using the equation below.

$$E_{RHE} = E_{Ag/AgCl} + 0.059 \times pH + E^0_{Ag/AgCl} \quad (1)$$

Where  $E_{RHE}$  is the converted potential vs. RHE.  $E_{Ag/AgCl}$  represents the experimental result vs.  $Ag/AgCl$  and  $E^0_{Ag/AgCl}$  is 0.197 V at ambient temperature of 25 °C.

Applied bias photon-to-current efficiency (ABPE) was calculated using the equation below.

$$ABPE (\%) = \frac{J \times (1.23 - V_b)}{P_{light}} \times 100\% \quad (2)$$

where  $J$  refers to the photocurrent density ( $mA\ cm^{-2}$ ) obtained from the electrochemical workstation.  $V_b$  represents the applied bias vs. RHE (V), and  $P_{light}$  is the total light intensity of AM 1.5 G ( $100\ mW\ cm^{-2}$ ).

Incident photon to electron conversion efficiency (IPCE) was measured using a motorized monochromator (M10; Jasco Corp.), which was calculated using the following equation.

$$IPCE (\%) = \frac{J \times 1240}{\lambda \times P_{light}} \times 100\% \quad (3)$$

where  $J$  is the photocurrent density ( $mA\ cm^{-2}$ ) obtained from the electrochemical workstation.  $\lambda$  and  $P_{light}$  refer to the incident light wavelength (nm) and the power density obtained at a specific wavelength ( $mW\ cm^{-2}$ ), respectively.

According to the Mott–Schottky curves, the flat-band potential ( $E_{fb}$ ) values were obtained from the intercept of the x-axis and the donor concentration ( $N_d$ ) can be calculated from the following equations.

$$N_d = \frac{2}{e\epsilon\epsilon_0} \times \left[ \frac{d\left[\frac{1}{C^2}\right]}{dV_s} \right]^{-1} \quad (4)$$

Where  $C$  denotes the space charge region's capacitance,  $e$  is electron charge and equal to  $1.6 \times 10^{-19}$  C,  $\epsilon \approx 80$  represents the dielectric constant of  $\alpha\text{-Fe}_2\text{O}_3$ , the vacuum permittivity of  $\epsilon_0$  is  $8.854 \times 10^{-14}$  F/cm and  $V$  is the applied potential on the photoanode.

The water oxidation photocurrent density could be calculated by the following formula,

$$J_{PEC} = J_{abs} \times \eta_{sep} \times \eta_{inj} \quad (5)$$

$J_{\text{abs}}$  is the photocurrent density when the absorbed photon completely converting into current. As a hole scavenger,  $\text{Na}_2\text{SO}_3$  can effectively trap the holes that arrived to the surface, without influencing the charge separation on the electrode ( $\eta_{\text{inj}}$  assumed to be 100%). Therefore, the charge separation efficiency in the bulk ( $\eta_{\text{sep}}$ ) and surface charge injection efficiency ( $\eta_{\text{inj}}$ ) could be deduced with following equations.

$$\eta_{\text{sep}} = \frac{J^{\text{Na}_2\text{SO}_3}}{J_{\text{abs}}} \quad (6)$$

$$\eta_{\text{inj}} = \frac{J^{\text{H}_2\text{O}}}{J^{\text{Na}_2\text{SO}_3}} \quad (7)$$

Where  $J^{\text{Na}_2\text{SO}_3}$  and  $J^{\text{H}_2\text{O}}$  are photocurrent densities obtained in 1 M NaOH electrolyte with and without 1 M  $\text{Na}_2\text{SO}_3$ , respectively. The  $J_{\text{abs}}$  was calculated by the overlapped areas between UV-vis absorption spectrum and AM 1.5G solar spectrum according to the following equation:

$$J_{\text{abs}} = \int \frac{\lambda}{1240} \cdot \varphi_{\text{AM 1.5G}}(\lambda) \cdot \text{LHE} \, d\lambda \quad (8)$$

$$\text{LHE} = 1 - 10^{-A(\lambda)} \quad (9)$$

Where  $\lambda$  is the wavelength (nm),  $\varphi_{\text{AM 1.5G}}(\lambda)$  provides the simulated solar spectral irradiance ( $\text{W m}^{-2} \text{nm}^{-1}$ ), LHE is the light harvesting efficiency,  $A(\lambda)$  is the absorbance at wavelength  $\lambda$ .

The experiment of gas evolution for water splitting was carried out in a completely sealed quartz reactor. The electrode with an area of  $1 \text{ cm}^2$  was immersed in the electrolyte in a three-electrode configuration. Prior to the reaction and sealing processes, the electrolyte was purged with argon gas. The generated  $\text{H}_2$  and  $\text{O}_2$  were analysed with a thermal conductivity detector (TCD) gas chromatograph (Shimadzu GC-8AIT, argon carrier). Similarly, AM 1.5 G solar simulation (WXS-80C-3 AM 1.5 G) with a light intensity of  $100 \text{ mW cm}^{-2}$  was utilized as the light sources directly without adding any light filter.

### Supporting Information

Supporting Information is available from the Wiley Online Library or from the author.

**Acknowledgements**

This work received financial support from the World Premier International Research Center Initiative (WPI Initiative) on Materials Nanoarchitectonics (MANA), MEXT, Japan.

Received: ((will be filled in by the editorial staff))

Revised: ((will be filled in by the editorial staff))

Published online: ((will be filled in by the editorial staff))

- [1] M. G. Walter, E. L. Warren, J. R. McKone, S. W. Boettcher, Q. Mi, E. A. Santori, N. S. Lewis, *Chem. Rev.* **2010**, *110*, 6446.
- [2] M. Grätzel, *Nature* **2001**, *414*, 338.
- [3] T. Hisatomi, J. Kubota, K. Domen, *Chem. Soc. Rev.* **2014**, *43*, 7520.
- [4] S. Kment, F. Riboni, S. Pausova, L. Wang, L. Wang, H. Han, Z. Hubicka, J. Krysa, P. Schmuki, R. Zboril, *Chem. Soc. Rev.* **2017**, *46*, 3716.
- [5] J. R. Swierk, T. E. Mallouk, *Chem. Soc. Rev.* **2013**, *42*, 2357.
- [6] K. Sivula, F. Le Formal, M. Grätzel, *ChemSusChem* **2011**, *4*, 432.
- [7] Y. Lin, G. Yuan, S. Sheehan, S. Zhou, D. Wang, *Energy Environ. Sci.* **2011**, *4*, 4862.
- [8] A. Kay, I. Cesar, M. Grätzel, *J. Am. Chem. Soc.* **2006**, *128*, 15714.
- [9] P. Peerakiatkhajohn, J. H. Yun, H. Chen, M. Lyu, T. Butburee, L. Wang, *Adv. Mater.* **2016**, *28*, 6405.
- [10] Z. Luo, T. Wang, J. Zhang, C. Li, H. Li, J. Gong, *Angew. Chem. Int. Ed.* **2017**, *56*, 12878.
- [11] Y. Ling, G. Wang, D. A. Wheeler, J. Z. Zhang, Y. Li, *Nano Lett.* **2011**, *11*, 2119.
- [12] I. Cesar, A. Kay, J. A. Gonzalez Martinez, M. Grätzel, *J. Am. Chem. Soc.* **2006**, *128*, 4582.
- [13] N. Mirbagheri, D. Wang, C. Peng, J. Wang, Q. Huang, C. Fan, E. E. Ferapontova, *ACS Catal.* **2014**, *4*, 2006.
- [14] M. T. Mayer, Y. Lin, G. Yuan, D. Wang, *Acc. Chem. Res.* **2013**, *46*, 1558.
- [15] Q. Liu, J. He, T. Yao, Z. Sun, W. Cheng, S. He, Y. Xie, Y. Peng, H. Cheng, Y. Sun, *Nat. Commun.* **2014**, *5*, 5122.

- [16] L. Wang, N. T. Nguyen, X. Huang, P. Schmuki, Y. Bi, *Adv. Funct. Mater.* **2017**, *27*, 1703527.
- [17] Y. F. Xu, X. D. Wang, H. Y. Chen, D. B. Kuang, C. Y. Su, *Adv. Funct. Mater.* **2016**, *26*, 4414.
- [18] D. K. Zhong, M. Cornuz, K. Sivula, M. Grätzel, D. R. Gamelin, *Energy Environ. Sci.* **2011**, *4*, 1759.
- [19] Q. Yu, X. Meng, T. Wang, P. Li, J. Ye, *Adv. Funct. Mater.* **2015**, *25*, 2686.
- [20] C. G. Morales-Guio, M. T. Mayer, A. Yella, S. D. Tilley, M. Grätzel, X. Hu, *J. Am. Chem. Soc.* **2015**, *137*, 9927.
- [21] J. Yang, D. Wang, H. Han, C. Li, *Acc. Chem. Res.* **2013**, *46*, 1900.
- [22] Q. Rui, L. Wang, Y. Zhang, C. Feng, B. Zhang, S. Fu, H. Guo, H. Hu, Y. Bi, *J. Mater. Chem. A* **2018**, *6*, 7021.
- [23] C. Ding, J. Shi, Z. Wang, C. Li, *ACS Catal.* **2016**, *7*, 675.
- [24] M. P. Suryawanshi, U. V. Ghorpade, S. W. Shin, U. P. Suryawanshi, H. J. Shim, S. H. Kang, J. H. Kim, *Small* **2018**, *14*, 1801226.
- [25] W. Liu, H. Liu, L. Dang, H. Zhang, X. Wu, B. Yang, Z. Li, X. Zhang, L. Lei, S. Jin, *Adv. Funct. Mater.* **2017**, *27*, 1603904.
- [26] G. Wang, B. Wang, C. Su, D. Li, L. Zhang, R. Chong, Z. Chang, *J. Catal.* **2018**, *359*, 287.
- [27] J. S. Kim, B. Kim, H. Kim, K. Kang, *Adv. Energy Mater.* **2018**, *8*.
- [28] F. Li, J. Li, J. Zhang, L. Gao, X. Long, Y. Hu, S. Li, J. Jin, J. Ma, *ChemSusChem* **2018**, *11*, 2156.
- [29] Z. Yan, H. Sun, X. Chen, H. Liu, Y. Zhao, H. Li, W. Xie, F. Cheng, J. Chen, *Nat. Commun.* **2018**, *9*, 2373.
- [30] N. Li, Y. Tian, J. Zhao, J. Zhang, J. Zhang, W. Zuo, Y. Ding, *Appl. Catal. B: Environ.* **2017**, *214*, 126.

- [31] J. X. Feng, H. Xu, Y. T. Dong, S. H. Ye, Y. X. Tong, G. R. Li, *Angew. Chem. Int. Ed.* **2016**, *128*, 3758.
- [32] S. Wang, T. He, J. H. Yun, Y. Hu, M. Xiao, A. Du, L. Wang, *Adv. Funct. Mater.* **2018**, *28*, 1802685.
- [33] Y. Liang, H. Wang, J. Zhou, Y. Li, J. Wang, T. Regier, H. Dai, *J. Am. Chem. Soc.* **2012**, *134*, 3517.
- [34] R. Nie, J. Shi, W. Du, W. Ning, Z. Hou, F.-S. Xiao, *J. Mater. Chem. A* **2013**, *1*, 9037.
- [35] H. Kim, J. Park, I. Park, K. Jin, S. E. Jerng, S. H. Kim, K. T. Nam, K. Kang, *Nat. Commun.* **2015**, *6*, 8253.
- [36] M.-R. Gao, Y.-F. Xu, J. Jiang, Y.-R. Zheng, S.-H. Yu, *J. Am. Chem. Soc.* **2012**, *134*, 2930.
- [37] B. S. Yeo, A. T. Bell, *J. Am. Chem. Soc.* **2011**, *133*, 5587.
- [38] A. Grimaud, K. J. May, C. E. Carlton, Y.-L. Lee, M. Risch, W. T. Hong, J. Zhou, Y. Shao-Horn, *Nat. Commun.* **2013**, *4*, 2439.
- [39] S. Zhao, R. Jin, H. Abroshan, C. Zeng, H. Zhang, S. D. House, E. Gottlieb, H. J. Kim, J. C. Yang, R. Jin, *J. Am. Chem. Soc.* **2017**, *139*, 1077.
- [40] T. Tang, W.-J. Jiang, S. Niu, N. Liu, H. Luo, Y.-Y. Chen, S.-F. Jin, F. Gao, L.-J. Wan, J.-S. Hu, *J. Am. Chem. Soc.* **2017**, *139*, 8320.
- [41] E. Kecsenvity, B. z. Endrődi, P. t. S. Tóth, Y. Zou, R. A. Dryfe, K. Rajeshwar, C. Janáky, *J. Am. Chem. Soc.* **2017**, *139*, 6682.
- [42] J. Zhang, R. García-Rodríguez, P. Cameron, S. Eslava, *Energy Environ. Sci.* **2018**, *11*, 2972.
- [43] X. Cheng, S. Cao, Y. Huan, Z. Bai, M. Li, H. Wu, R. Zhang, W. Peng, Z. Ji, X. Yan, *Energy Technol.* **2019**, *7*, 1800899.
- [44] K. Zhang, B. Jin, C. Park, Y. Cho, X. Song, X. Shi, S. Zhang, W. Kim, H. Zeng, J. H. Park, *Nat. Commun.* **2019**, *10*, 2001.

- [45] F. A. Laskowski, M. R. Nellist, J. Qiu, S. W. Boettcher, *J. Am. Chem. Soc.* **2019**, *141*, 1394.
- [46] G. Liu, P. Li, G. Zhao, X. Wang, J. Kong, H. Liu, H. Zhang, K. Chang, X. Meng, T. Kako, *J. Am. Chem. Soc.* **2016**, *138*, 9128.
- [47] D. K. Zhong, D. R. Gamelin, *J. Am. Chem. Soc.* **2010**, *132*, 4202.
- [48] A. Indra, P. W. Menezes, N. R. Sahraie, A. Bergmann, C. Das, M. Tallarida, D. Schmeißer, P. Strasser, M. Driess, *J. Am. Chem. Soc.* **2014**, *136*, 17530.
- [49] D. Zhao, Y. Pi, Q. Shao, Y. Feng, Y. Zhang, X. Huang, *ACS Nano* **2018**, *12*, 6245.

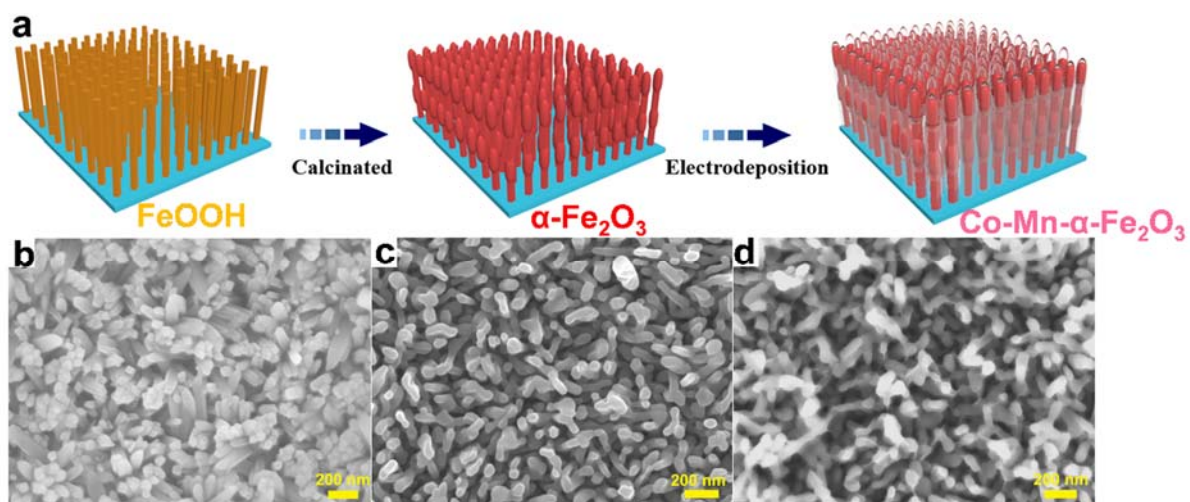


**Figure 1.** a) Scheme of fabrication processes of  $\alpha$ -Fe<sub>2</sub>O<sub>3</sub> films and electrodeposition procedures of ultrathin Co-Mn nanosheets; top-view SEM images of b) FeOOH, c)  $\alpha$ -Fe<sub>2</sub>O<sub>3</sub>, d) Co-Mn- $\alpha$ -Fe<sub>2</sub>O<sub>3</sub>.

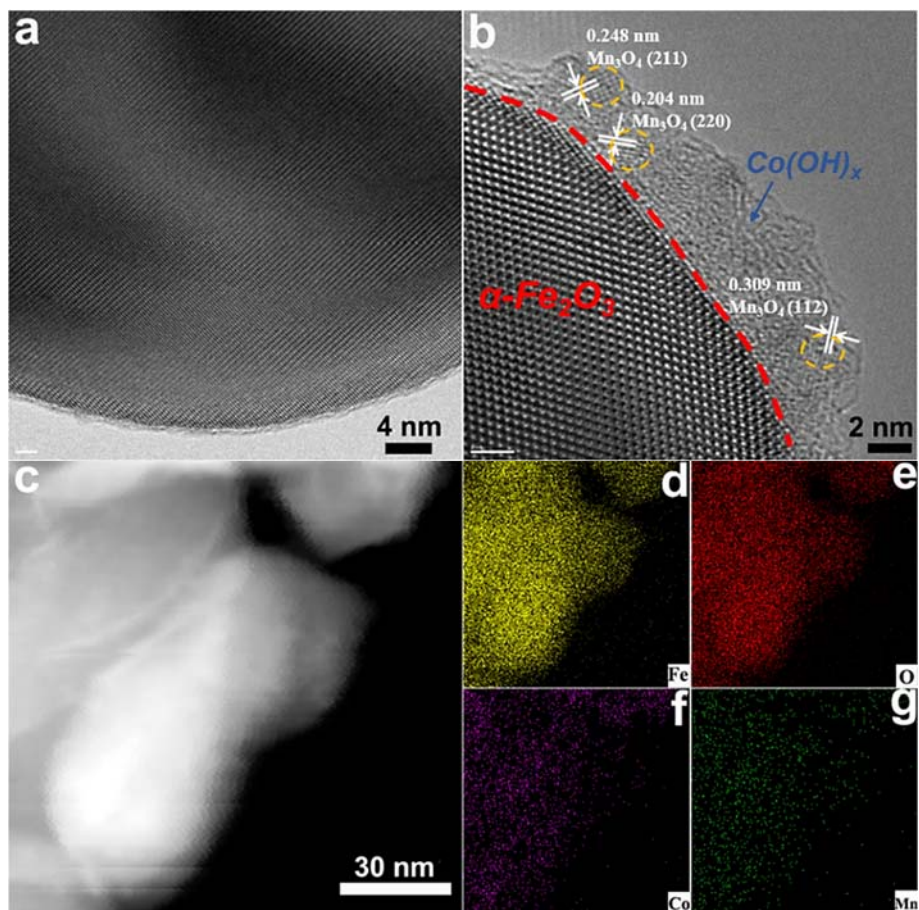


**Figure 2.** (a) TEM image, (b) HRTEM image, (c-g) EDS elemental mapping images of Co-Mn- $\alpha$ -Fe<sub>2</sub>O<sub>3</sub> refer to the signals of Fe, O, Co and Mn, respectively.

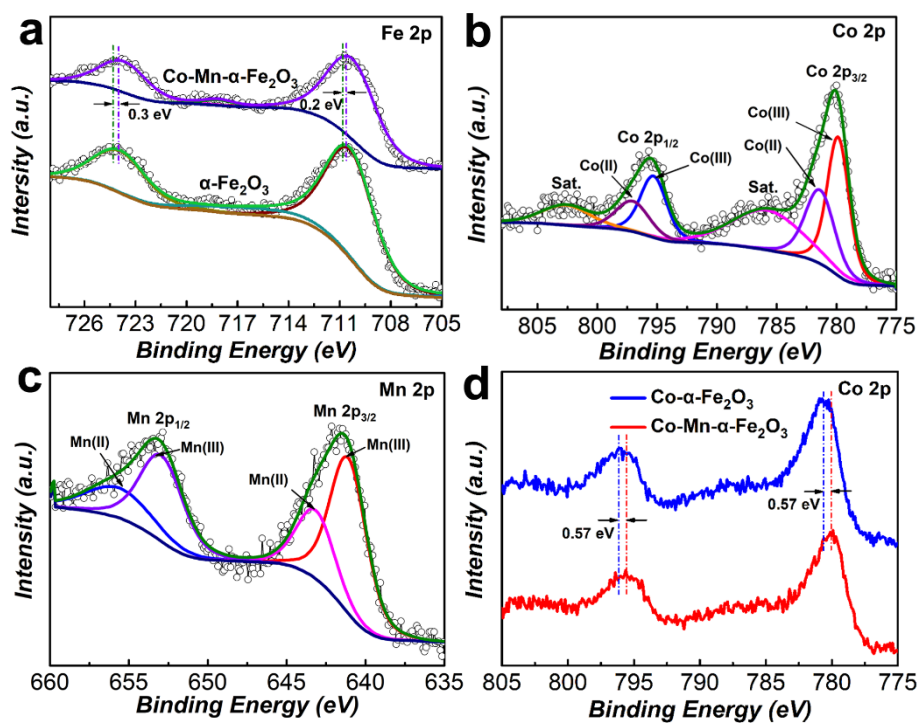


**Figure 3.** (a) Fe 2p XPS spectra of  $\alpha\text{-Fe}_2\text{O}_3$  and Co-Mn- $\alpha\text{-Fe}_2\text{O}_3$ , (b) Co 2p and (c) Mn 2p XPS spectra of Co-Mn- $\alpha\text{-Fe}_2\text{O}_3$ , (d) Co 2p XPS spectra of Co- $\alpha\text{-Fe}_2\text{O}_3$  and Co-Mn- $\alpha\text{-Fe}_2\text{O}_3$ .

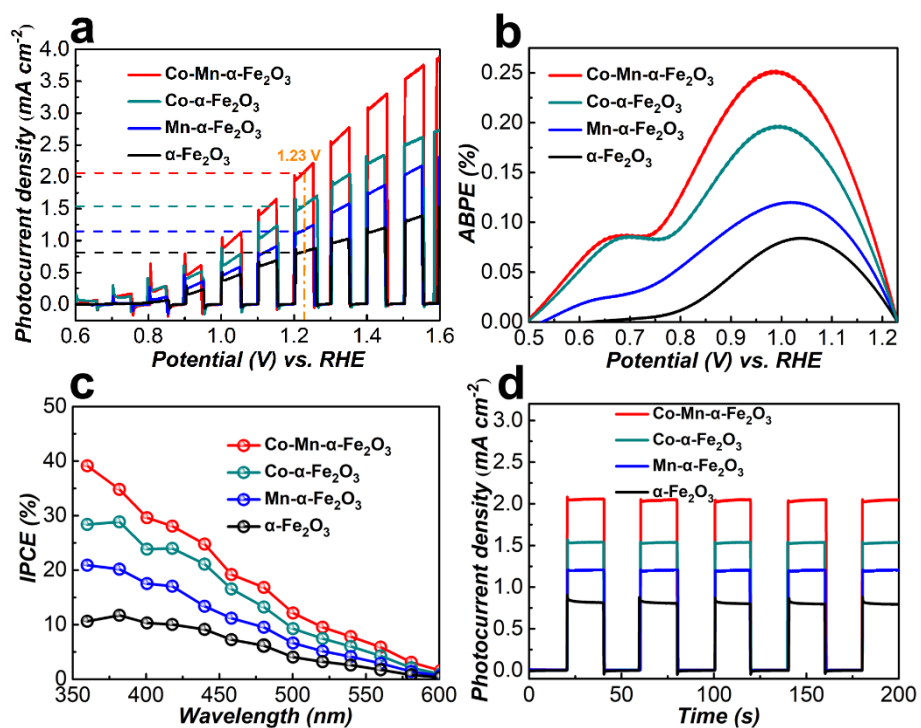


**Figure 4.** (a)  $J$ - $V$  curves, (b) ABPE curves, (c) IPCE curves and (d) current-time curves of pristine  $\alpha\text{-Fe}_2\text{O}_3$ ,  $\text{Mn-}\alpha\text{-Fe}_2\text{O}_3$  (decorated with Mn compound),  $\text{Co-}\alpha\text{-Fe}_2\text{O}_3$  (decorated with Co compound) and  $\text{Co-Mn-}\alpha\text{-Fe}_2\text{O}_3$  photoanodes. The IPCE and current-time curves were measured at 1.23 V vs. RHE under AM 1.5 G illumination.

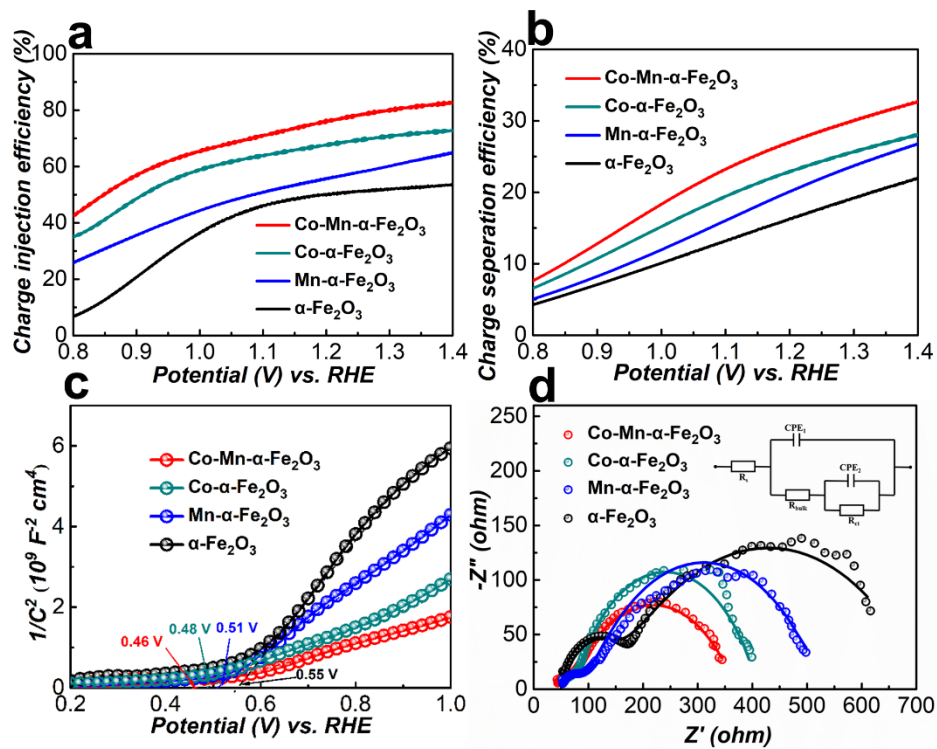


**Figure 5.** a) Charge injection efficiencies on the surface, b) charge separation efficiencies in the bulk, c) Mott-Schottky plots and d) EIS plots and fitting-figures (solid lines) of pristine  $\alpha$ -Fe<sub>2</sub>O<sub>3</sub>, Mn- $\alpha$ -Fe<sub>2</sub>O<sub>3</sub>, Co- $\alpha$ -Fe<sub>2</sub>O<sub>3</sub> and Co-Mn- $\alpha$ -Fe<sub>2</sub>O<sub>3</sub> photoanodes.

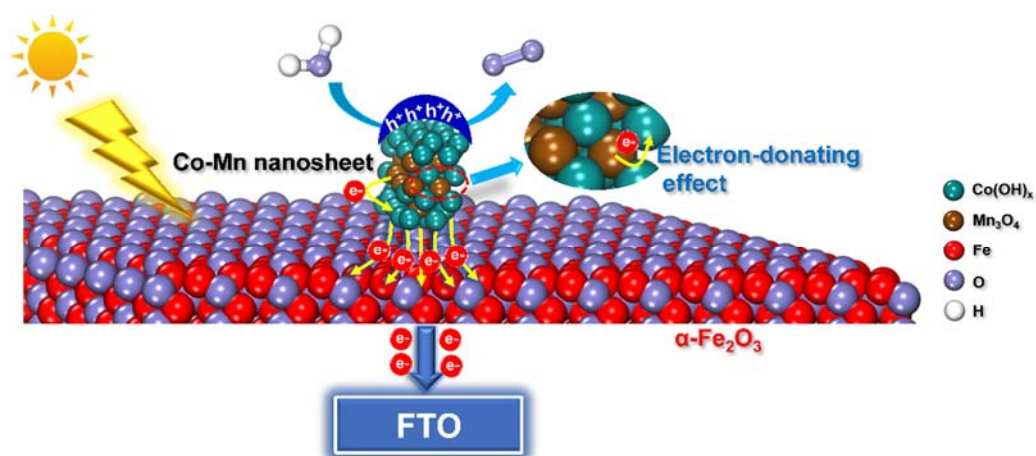


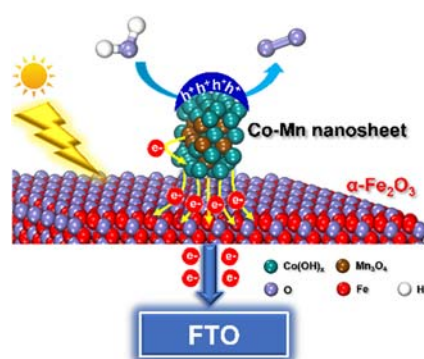
**Figure 6.** Schematic electron transfer paths presumed to occur in Co-Mn- $\alpha$ -Fe<sub>2</sub>O<sub>3</sub> photoanode under AM 1.5 G illumination responsible for the PEC water oxidation.

An ultrathin cobalt-manganese (Co-Mn) nanosheet is designed as an efficient co-catalyst on  $\alpha$ - $\text{Fe}_2\text{O}_3$  film for photoelectrochemical water oxidation. Incorporation of Mn sites in the nanosheets could create electron donation to Co sites and facilitate the generation of key intermediates, which drastically increases the catalytic activities for oxygen evolution reaction.

**Keyword** (Cobalt-manganese nanosheets, electron-donating effect, photoelectrocatalysis, water oxidation)

*Gaoliang Yang, Yunxiang Li, Hong Pang, Kun Chang, and Jinhua Ye\**

### Ultrathin Cobalt-Manganese Nanosheets: An Efficient Platform for Enhanced Photoelectrochemical Water Oxidation with Electron-Donating Effect



## Supporting Information

### **Ultrathin Cobalt-Manganese Nanosheets: An Efficient Platform for Enhanced Photoelectrochemical Water Oxidation with Electron-Donating Effect**

*Gaoliang Yang, Yunxiang Li, Hong Pang, Kun Chang, and Jinhua Ye\**

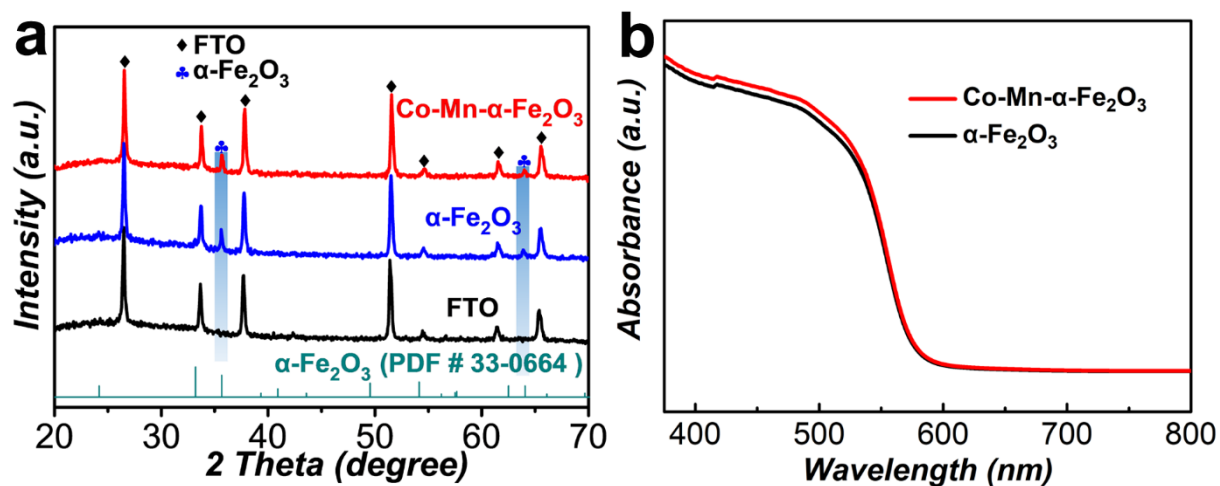


**Figure S1.** (a) XRD patterns of Co-Mn- $\alpha$ -Fe<sub>2</sub>O<sub>3</sub>,  $\alpha$ -Fe<sub>2</sub>O<sub>3</sub> and FTO, (b) UV-visible diffuse reflection spectra of Co-Mn- $\alpha$ -Fe<sub>2</sub>O<sub>3</sub> and  $\alpha$ -Fe<sub>2</sub>O<sub>3</sub>.

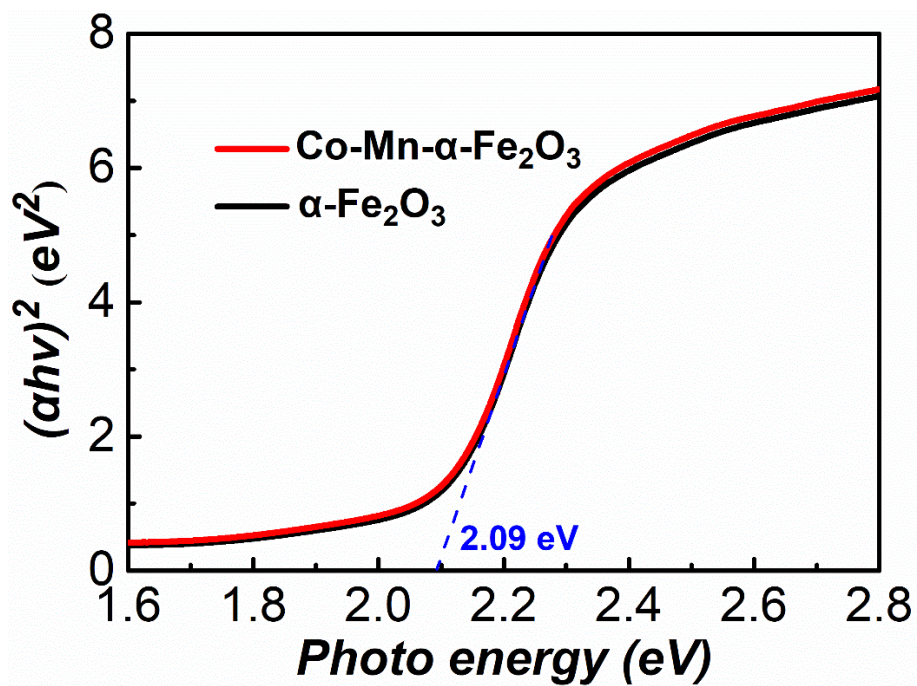


**Figure S2.** Tauc plots of Co-Mn- $\alpha$ - $\text{Fe}_2\text{O}_3$  and  $\alpha$ - $\text{Fe}_2\text{O}_3$ .

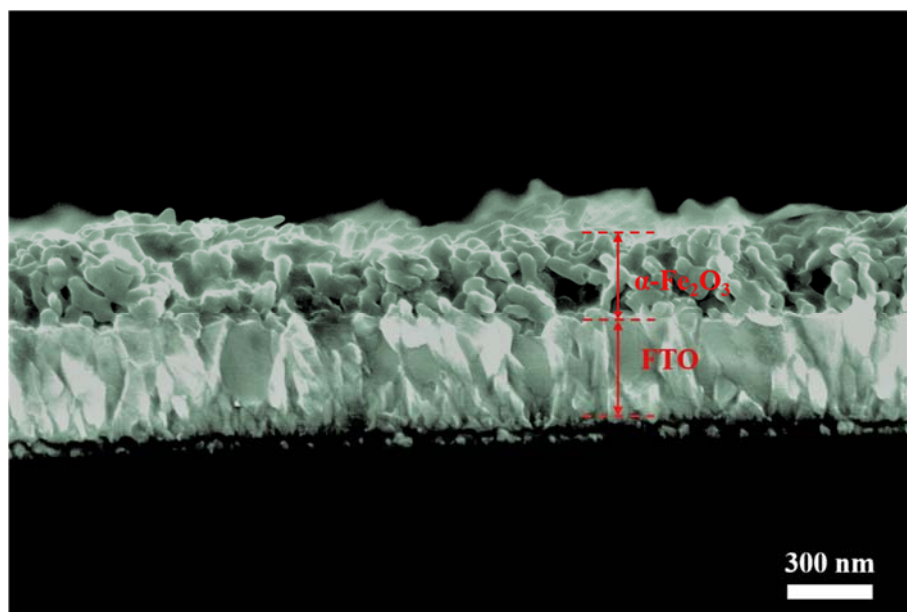


**Figure S3.** Cross-section SEM image of  $\alpha\text{-Fe}_2\text{O}_3$  nanorods.

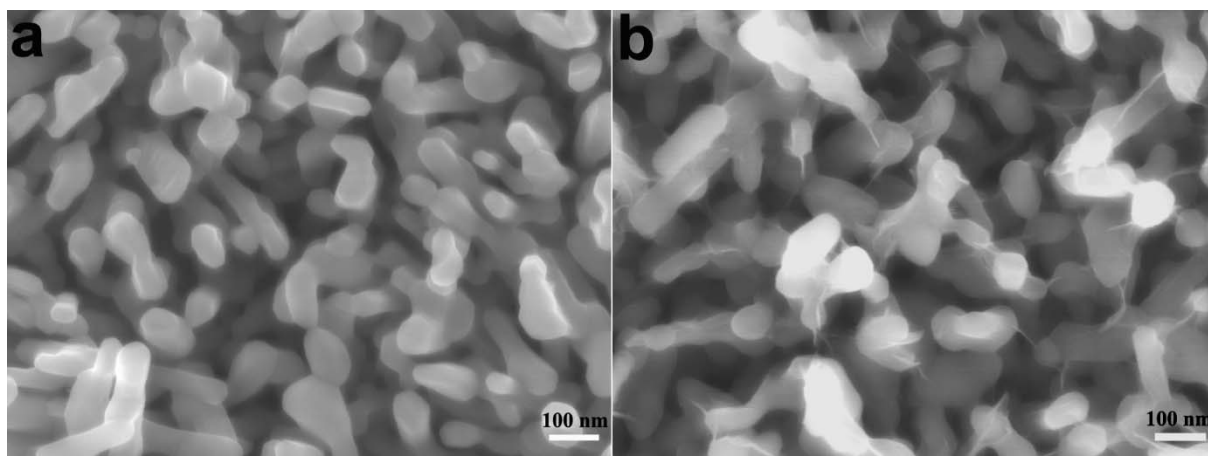


**Figure S4.** Top-view SEM images with larger magnification of (a)  $\alpha$ - $\text{Fe}_2\text{O}_3$ , (b) Co-Mn- $\alpha$ - $\text{Fe}_2\text{O}_3$ .

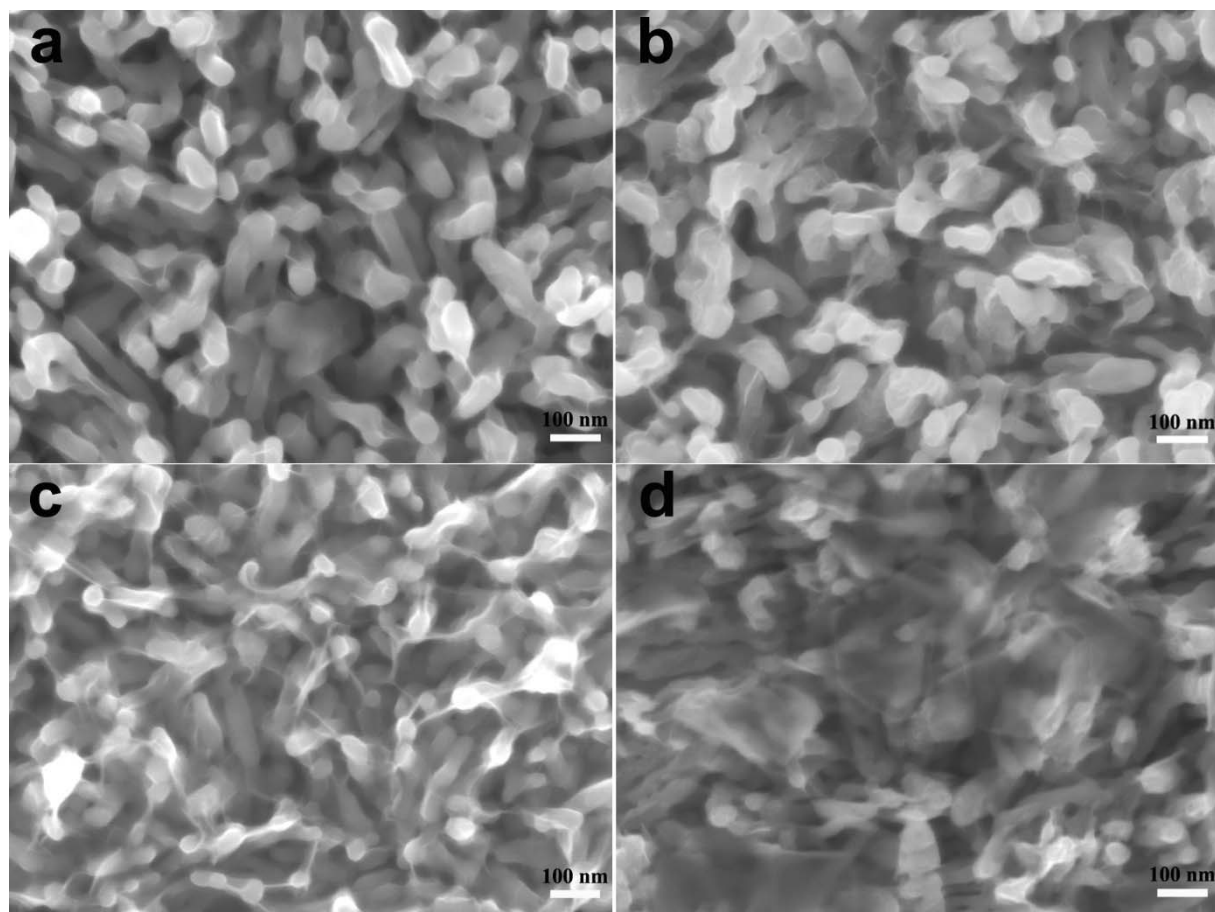


**Figure S5.** Time-dependent SEM images of the Co-Mn- $\alpha$ -Fe<sub>2</sub>O<sub>3</sub> films obtained at electro-deposition of (a) 15 s, (b) 60 s, (c) 90 s, (d) 120 s, respectively.

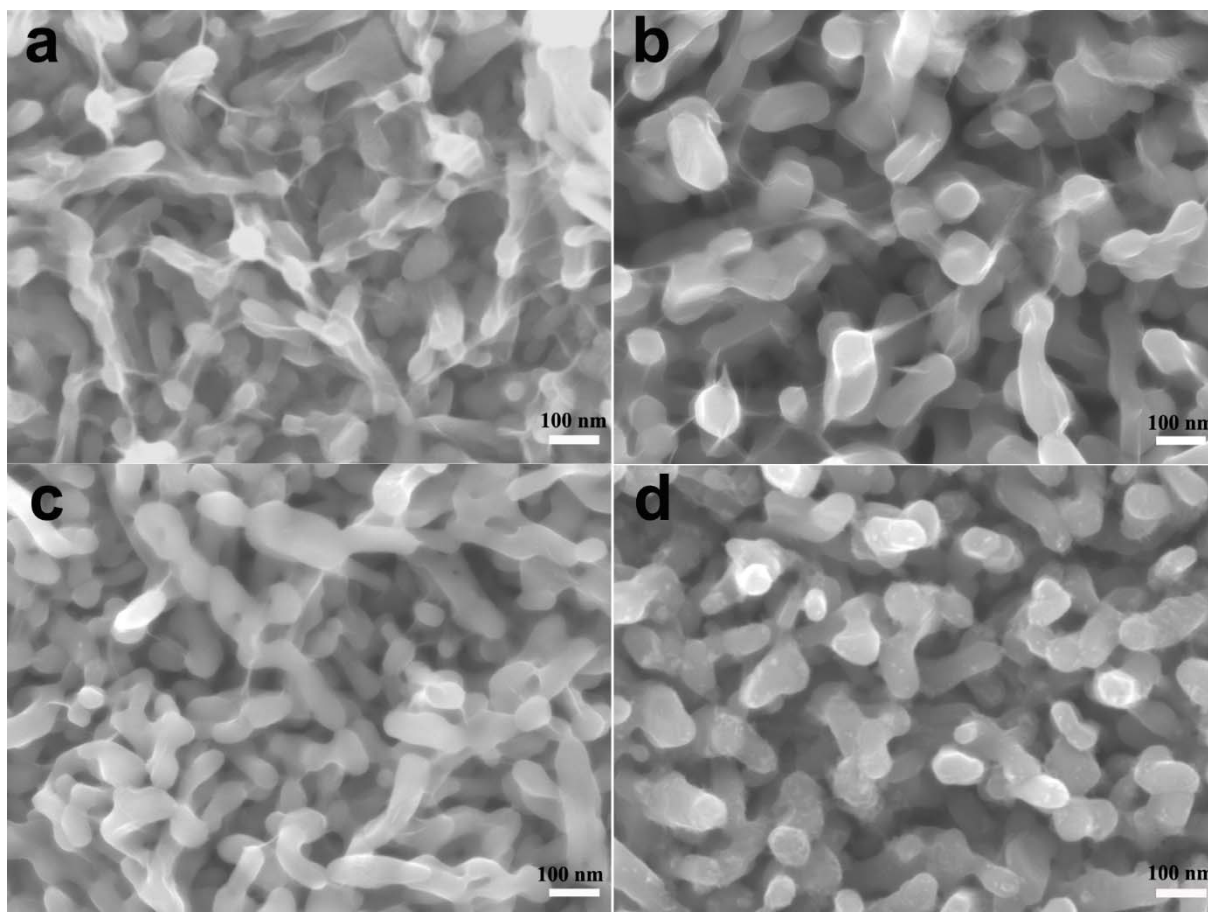


**Figure S6.** SEM images of films electrodeposited with different Co-Mn ratio: (a) Co- $\alpha$ -Fe<sub>2</sub>O<sub>3</sub>, (b) Co<sub>0.75</sub>-Mn<sub>0.25</sub>- $\alpha$ -Fe<sub>2</sub>O<sub>3</sub>, (c) Co<sub>0.25</sub>-Mn<sub>0.75</sub>- $\alpha$ -Fe<sub>2</sub>O<sub>3</sub> and (d) Mn- $\alpha$ -Fe<sub>2</sub>O<sub>3</sub>.

To optimize the Co-Mn nanosheets, contrast experiments with different time and varied Co-Mn ratio were carried out to investigate the morphological evolution of modified films. It can be observed that inconspicuous change in morphology (with few nanosheets coated on  $\alpha$ -Fe<sub>2</sub>O<sub>3</sub>) is observed with electrodeposition time of 15 s (Figure S5a). With electrodeposition time increasing to 60 s, nanosheets on the surface of  $\alpha$ -Fe<sub>2</sub>O<sub>3</sub> nanorods become somewhat obvious (Figure S5b). A much more intensive coating layer grows on the surface of  $\alpha$ -Fe<sub>2</sub>O<sub>3</sub> nanorods with electrodeposition time of 90 s (Figure S5c). When the reaction time increases to 120 s, the whole surface of  $\alpha$ -Fe<sub>2</sub>O<sub>3</sub> nanorods is densely covered by the overlayer of Co-Mn nanosheets, which may hinder the light capture and the transport of photo-induced charge carriers. In order to investigate the influence of Co and Mn on the morphology of the nanosheets, we further varied Co and Mn ratio in the precursor solution with optimized electrodeposition time of 30 s.

Different morphologies of films electrodeposited with different Co-Mn ratios are shown in Figure S6. Element of Co is conducive to form nanosheets covered on the surface of  $\alpha$ -Fe<sub>2</sub>O<sub>3</sub> nanorods. The more ratio of Co added, the more obvious and thicker nanosheets formed. If only the Mn element exists, the nanosheets morphology would be hardly developed (Figure S6d). The result is consistent with HRTEM images, which presented that Co element formed the amorphous nanosheets of Co(OH)<sub>x</sub>, while Mn element transformed to Mn<sub>3</sub>O<sub>4</sub> nanocrystals during the electrodeposition.

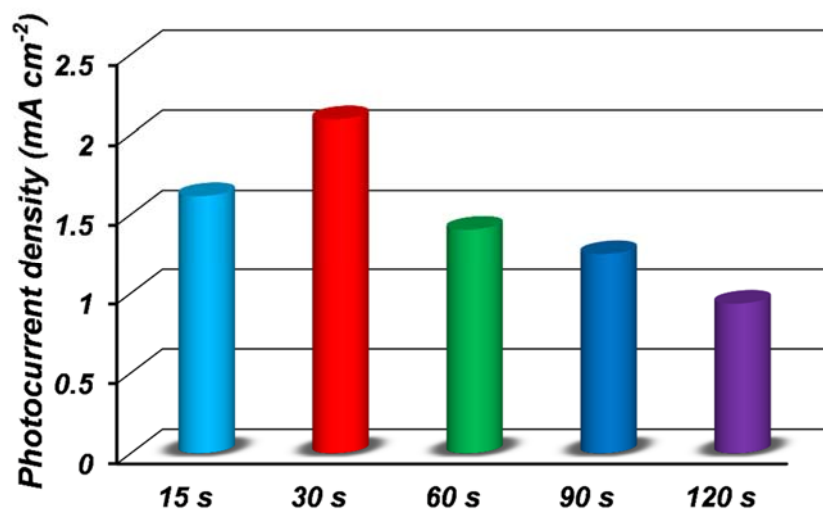


**Figure S7.** Photocurrent densities of Co-Mn- $\alpha$ -Fe<sub>2</sub>O<sub>3</sub> films electrodeposited for 15 s, 30 s, 60 s, 90 s and 120 s at 1.23 V vs. RHE under AM 1.5 G illumination.

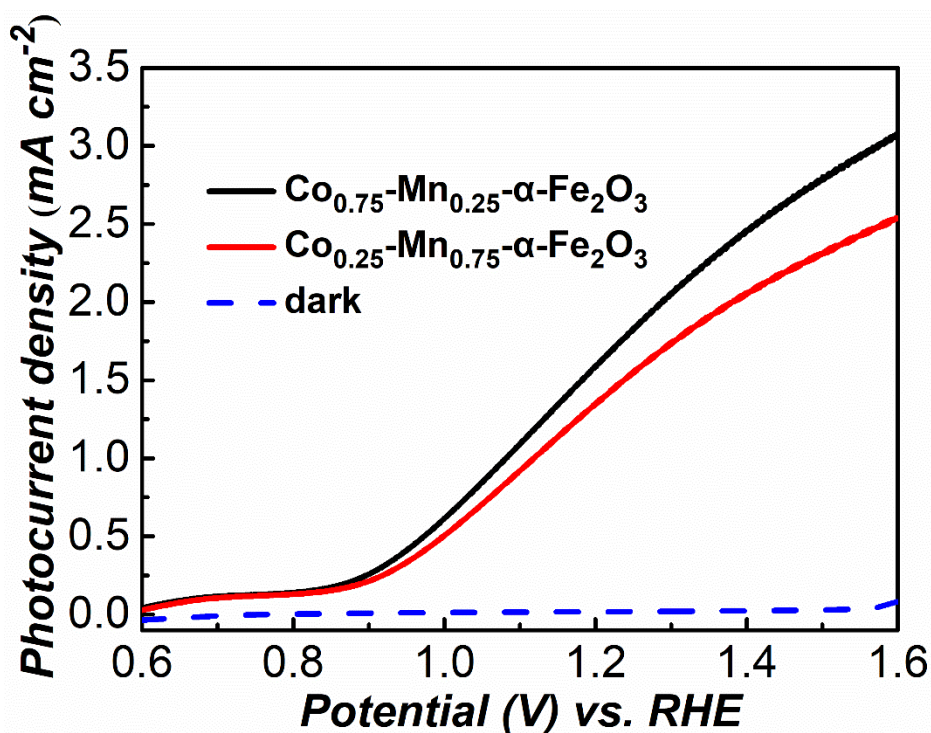


**Figure S8.**  $J$ - $V$  curves of the  $\text{Co}_{0.75}\text{-Mn}_{0.25}\text{-}\alpha\text{-Fe}_2\text{O}_3$  and  $\text{Co}_{0.25}\text{-Mn}_{0.75}\text{-}\alpha\text{-Fe}_2\text{O}_3$ .

By comparing visual activity (the photocurrent densities at 1.23 V vs. RHE obtained from  $J$ - $V$  curves), optimized electrodeposition time and Co-Mn ratio in precursor solution could be acquired. As shown in Figure S7, the activities of Co-Mn- $\alpha$ -Fe<sub>2</sub>O<sub>3</sub> photoanodes with different electrodeposition time were evaluated. It was revealed that Co-Mn- $\alpha$ -Fe<sub>2</sub>O<sub>3</sub> photoanode with electrodeposition time of 30 s presents the highest photocurrent density. After then, the continue increase of electrodeposition time from 30 s would lead to a negative effect on photocurrent densities of the photoanodes, which may due to intensive covering of Co-Mn nanosheets over  $\alpha$ -Fe<sub>2</sub>O<sub>3</sub> nanorods (Figure S5). As shown in Figure S8, the photocurrent densities of  $\text{Co}_{0.75}\text{-Mn}_{0.25}\text{-}\alpha\text{-Fe}_2\text{O}_3$  (the ratio of Co and Mn in precursor solution is 0.75:0.25) and  $\text{Co}_{0.25}\text{-Mn}_{0.75}\text{-}\alpha\text{-Fe}_2\text{O}_3$  (the ratio of Co and Mn in precursor solution is 0.25:0.75) are 1.75 and 1.47 mA cm<sup>-2</sup> at 1.23 V vs. RHE, respectively.

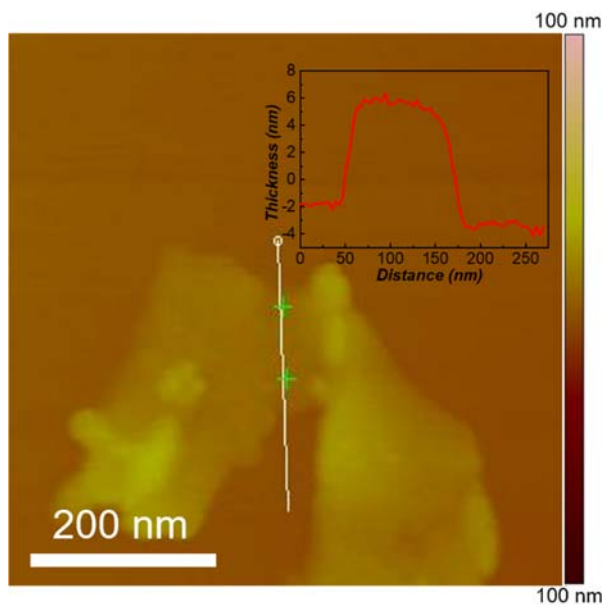


**Figure S9.** AFM image of ultrathin Co-Mn nanosheet. Inset of AFM image shows the height profile along the white line.

There exist two possible structures for these two phases, in which the nanocrystals are embedded within the matrix of amorphous layer or loaded on top of the layer surface (without being embedded). In order to further verify the exact structure, atomic force microscopy (AFM) was used to reveal the surface state of the Co-Mn nanosheets. Figure S9 shows that the surface of the nanosheet is relatively smooth, without any obvious presence of nanocrystals. Moreover, the height statistics unveil that the thickness of the nanosheet is about 7 nm, which keeps nearly unchanged along the white line on the nanosheet. As expected, the AFM results verified that the  $\text{Mn}_3\text{O}_4$  nanocrystals are indeed embedded in the matrix of  $\text{Co}(\text{OH})_x$  amorphous layer, rather than locating on top of the layer surface (without being embedded).

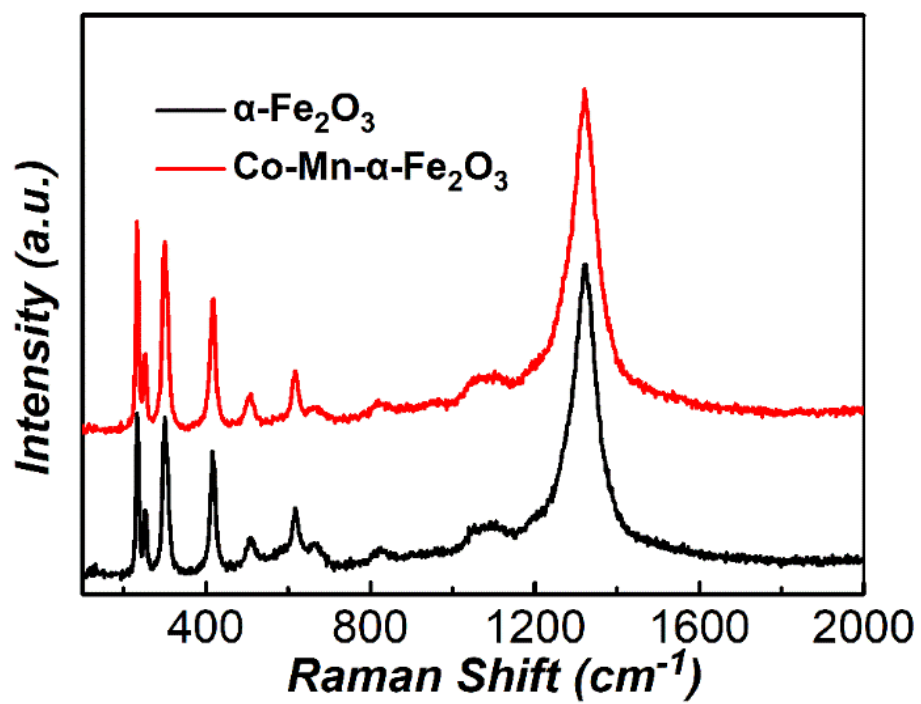


**Figure S10.** Raman spectra of  $\alpha\text{-Fe}_2\text{O}_3$  and  $\text{Co-Mn-}\alpha\text{-Fe}_2\text{O}_3$ .

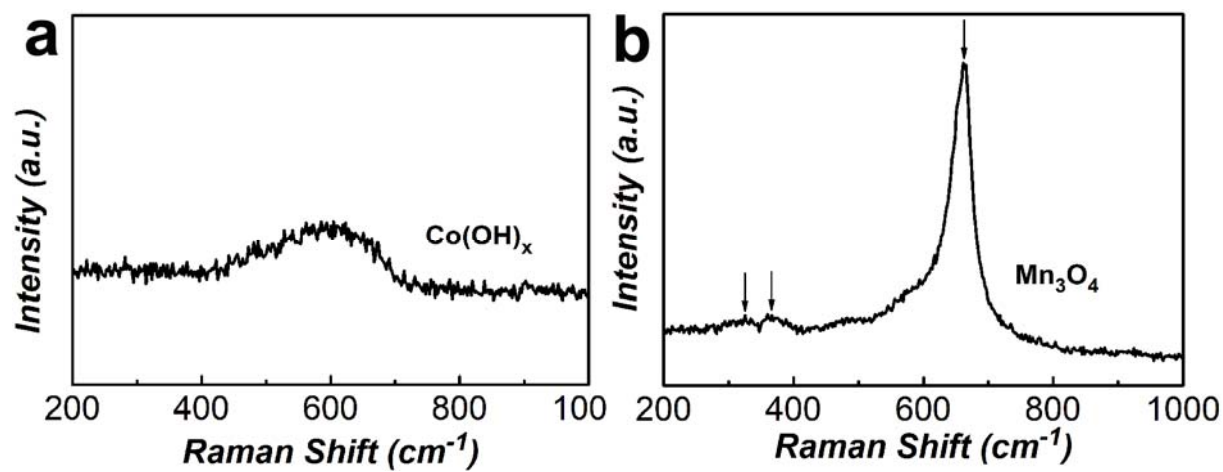


**Figure S11.** Raman spectra of (a)  $\text{Co(OH)}_x$  and (b)  $\text{Mn}_3\text{O}_4$  deposited on FTO substrate.

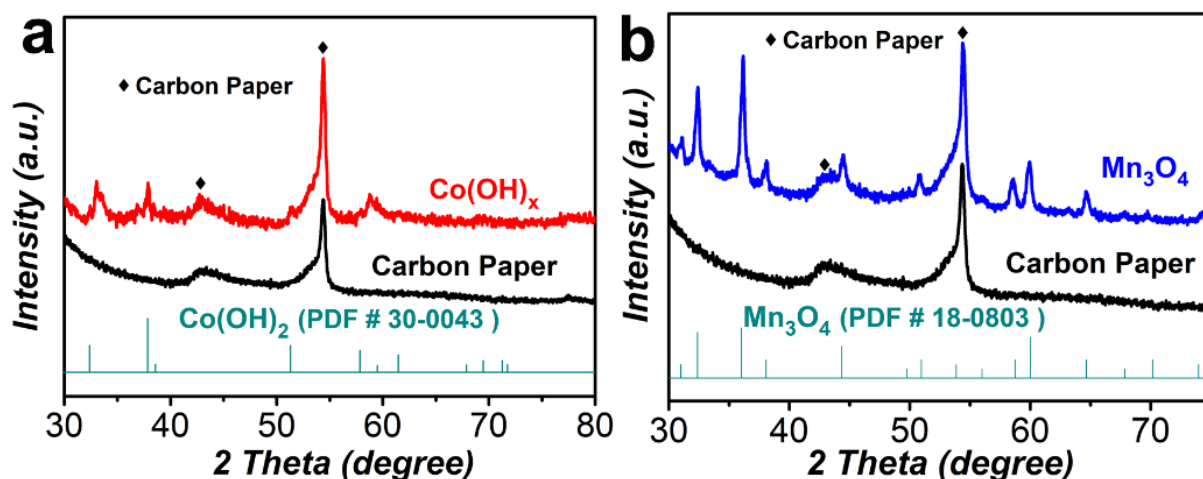


**Figure S12.** XRD patterns of (a)  $\text{Co(OH)}_x$  and (b)  $\text{Mn}_3\text{O}_4$  deposited on carbon paper substrate

The TEM test results in Figure 2 have confirmed that the Co-Mn nanosheets are composed by amorphous layers and ultras-small nanocrystals. In order to have a more convincing and deep understanding about the structure of the materials, some additional characterizations have been conducted. Firstly, Raman spectra of the  $\alpha\text{-Fe}_2\text{O}_3$  and Co-Mn- $\alpha\text{-Fe}_2\text{O}_3$  are presented in Figure S10. All the peaks are corresponded well with each other for these two materials, which could be indexed with the  $\alpha\text{-Fe}_2\text{O}_3$  grown on FTO (J. Phys. Chem. B, **2005**, 109, 17184). Similar with the results of XRD patterns, no signals of Co-Mn nanosheets were detected in the Raman spectra. The reason may be attributed to the strong signals of  $\alpha\text{-Fe}_2\text{O}_3$ , which would cover the weak signals of Co-Mn nanosheets (the signals of Co-Mn nanosheets are close to  $\alpha\text{-Fe}_2\text{O}_3$ ). In order to eliminate the influence of  $\alpha\text{-Fe}_2\text{O}_3$  and mutual influence between Co compound and Mn compound, the Co and Mn compounds were deposited on the FTO separately, which might be easier and more accurate to investigate their structures. In this case, the same method and parameters were used to deposit the Co and Mn compounds on FTO substrate separately. The Raman spectrum in Figure S11a shows that only one broad peak is obtained with Co compound on FTO substrate, which indicates the amorphous property (consistent with the TEM test). The Raman spectrum of Mn compound in Figure S11b is well indexed to the reported  $\text{Mn}_3\text{O}_4$  structure (J. Mater. Chem. A, **2014**, 2, 17477-17488; Int. J. Electrochem. Sci, 2012, 7, 7440-7450), which is also in accordance with the TEM result. Due to the amorphous property of Co

compound deposited on the FTO substrate, the carbon paper was selected as the substrate (Nat. Commun. **2018**, 9, 2373), which may lead to better crystallinity. As shown in Figure S12, the Co compound is well attributed to  $\text{Co(OH)}_2$  crystal structure (PDF # 30-0043) and the Mn compound is adequately indexed to  $\text{Mn}_3\text{O}_4$  crystal structure (PDF # 18-0803). It is interesting that the  $\text{Co(OH)}_x$  presents different crystallinity with different substrates, which is agree well with the reported results with the similar electrodeposition method (Nat. Commun. **2018**, 9, 2373 (carbon paper); Adv. Funct. Mater. **2017**, 27, 1603904 (FTO)). The different crystallinity may be attributed to the different conductivity and roughness of the substrates, which would affect formation mechanism of the compounds.

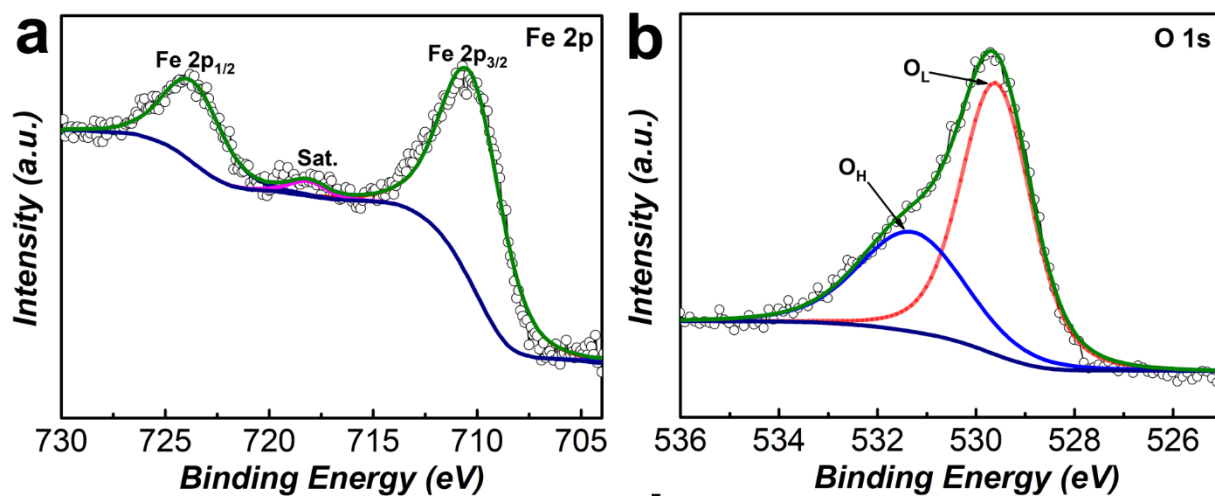


**Figure S13.** (a) Fe 2p and (b) O 1s XPS spectra of Co-Mn- $\alpha$ -Fe<sub>2</sub>O<sub>3</sub>.

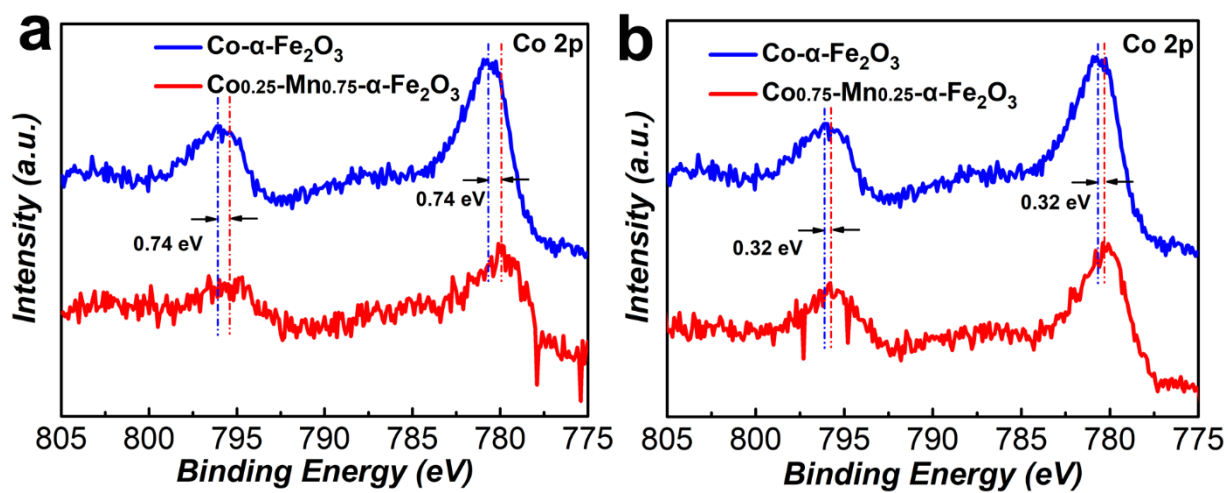


**Figure S14.** Co 2p XPS spectra of (a) Co- $\alpha$ -Fe<sub>2</sub>O<sub>3</sub> and Co<sub>0.25</sub>Mn<sub>0.75</sub>- $\alpha$ -Fe<sub>2</sub>O<sub>3</sub>, (b) Co- $\alpha$ -Fe<sub>2</sub>O<sub>3</sub> and Co<sub>0.75</sub>Mn<sub>0.25</sub>- $\alpha$ -Fe<sub>2</sub>O<sub>3</sub>.

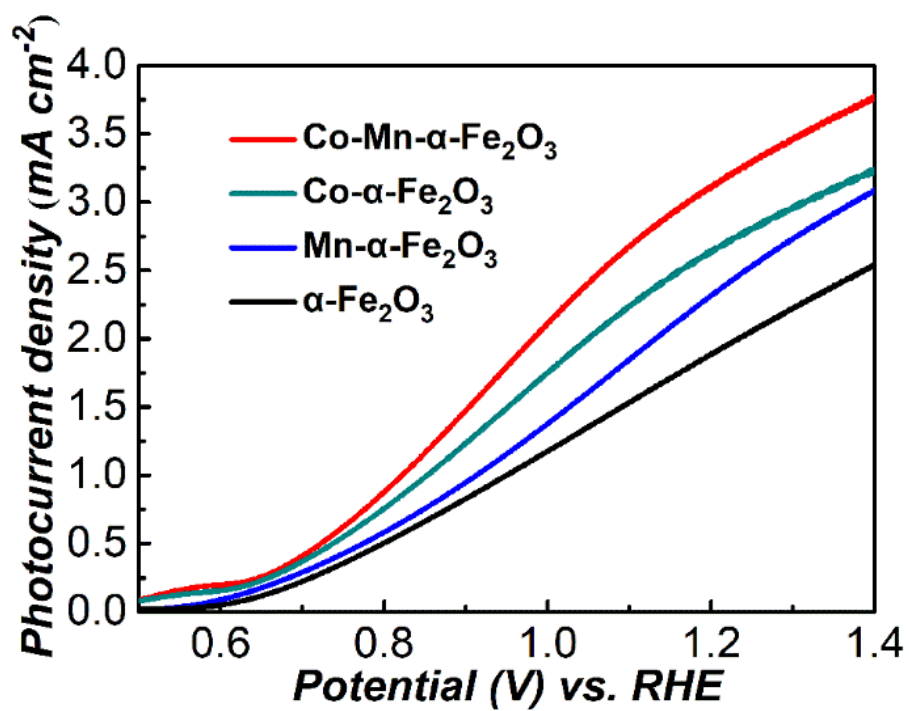


**Figure S15.**  $J$ - $V$  curves of pristine  $\alpha$ -Fe<sub>2</sub>O<sub>3</sub>, Mn- $\alpha$ -Fe<sub>2</sub>O<sub>3</sub>, Co- $\alpha$ -Fe<sub>2</sub>O<sub>3</sub> and Co-Mn- $\alpha$ -Fe<sub>2</sub>O<sub>3</sub> photoanodes with Na<sub>2</sub>SO<sub>3</sub> as the hole scavenger.

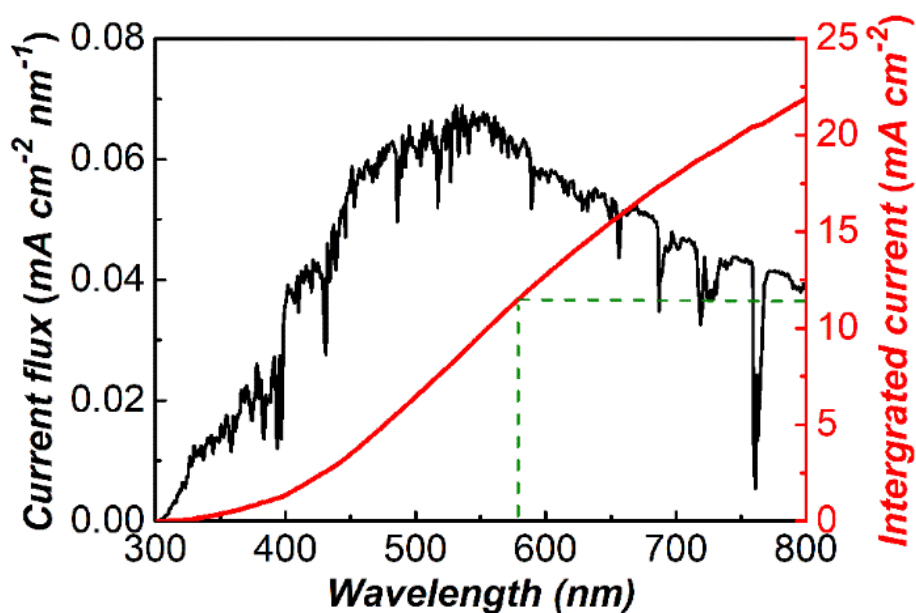


**Figure S16.** The calculated current density flux and integrated current density ( $J_{\text{abs}}$ ) of Co-Mn- $\alpha$ - $\text{Fe}_2\text{O}_3$  photoanode.

According to the result of UV-vis spectra, the optional properties of hematite films would not be changed by the decoration of Co-Mn nanosheets. The light absorption edge of Co-Mn- $\alpha$ - $\text{Fe}_2\text{O}_3$  is around 580 nm and the bandgap is calculated to be 2.09 eV (Tauc plots in Figure S2). Thus, the  $J_{\text{abs}}$  could be calculated to be 11.5  $\text{mA cm}^{-2}$  according to the equation 8 in experimental section.”

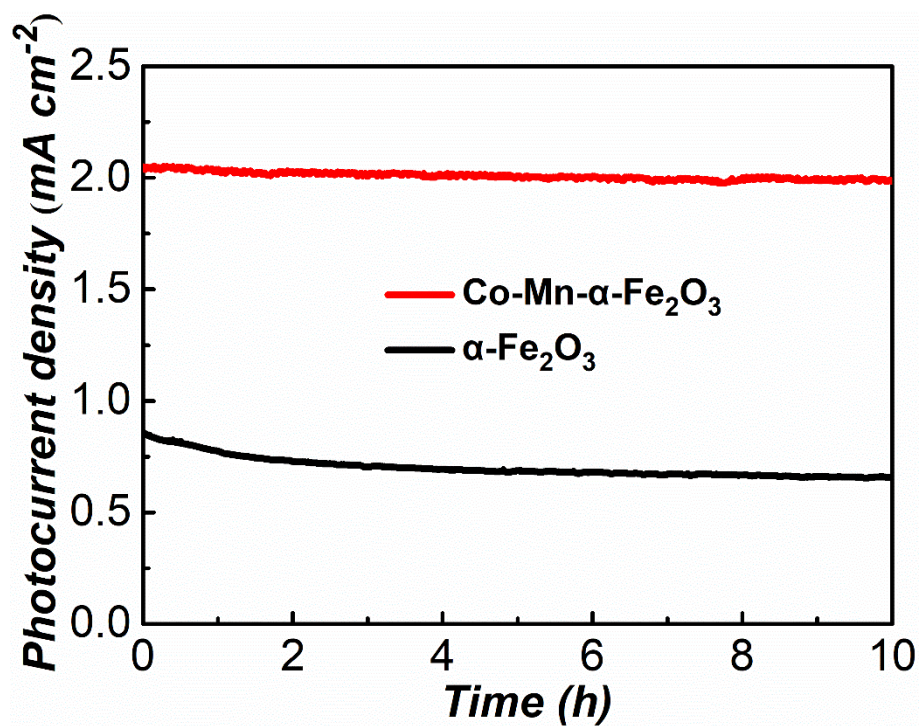


**Figure S17.** Stability test of  $\alpha$ -Fe<sub>2</sub>O<sub>3</sub> and Co-Mn- $\alpha$ -Fe<sub>2</sub>O<sub>3</sub> photoanodes for 10 h.

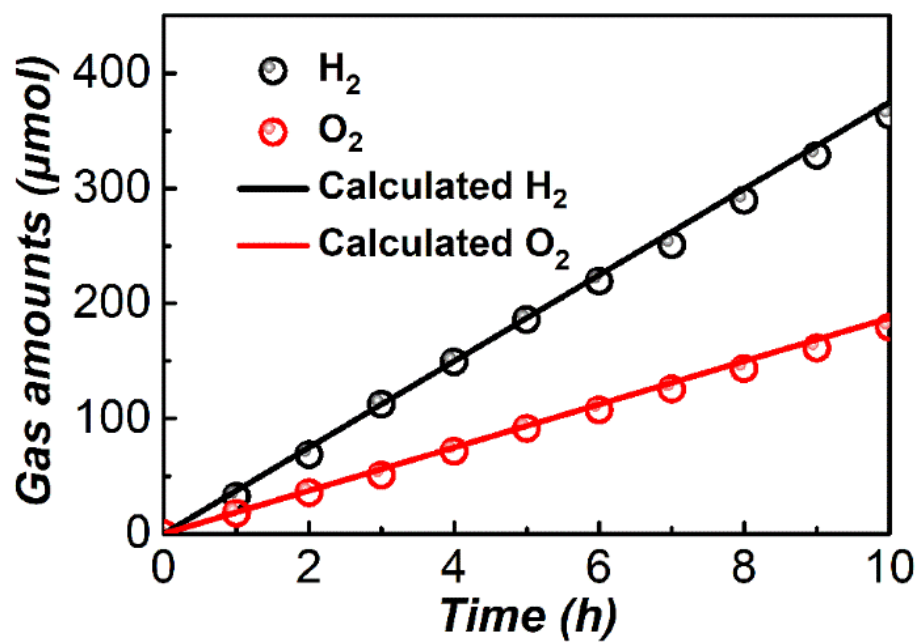


**Figure S18.** Gas evolution curves for Co-Mn- $\alpha$ -Fe<sub>2</sub>O<sub>3</sub> photoanode under AM 1.5 G illumination at 1.23 V vs. RHE.

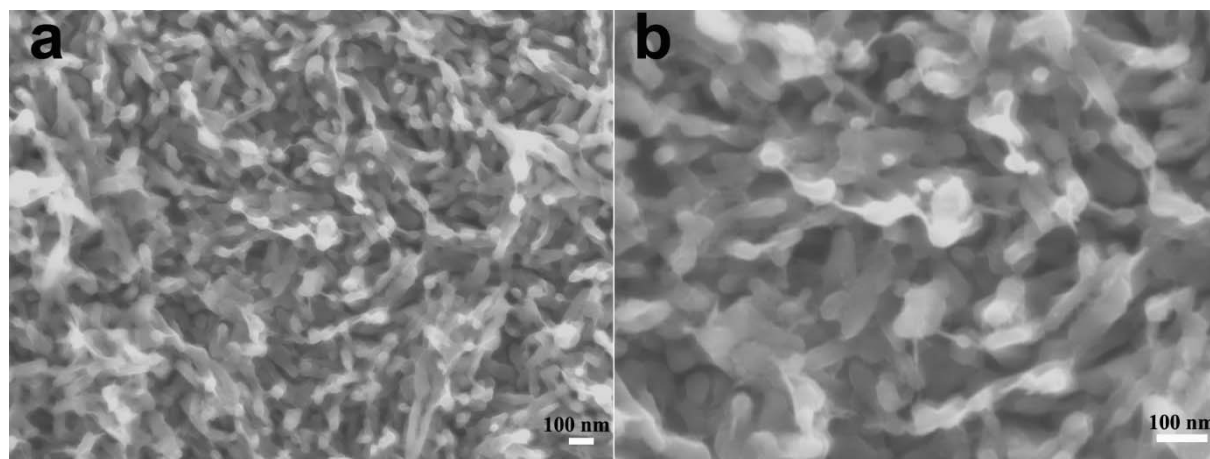


**Figure S19.** SEM images of the Co-Mn- $\alpha$ -Fe<sub>2</sub>O<sub>3</sub> films after stability test with different magnification.

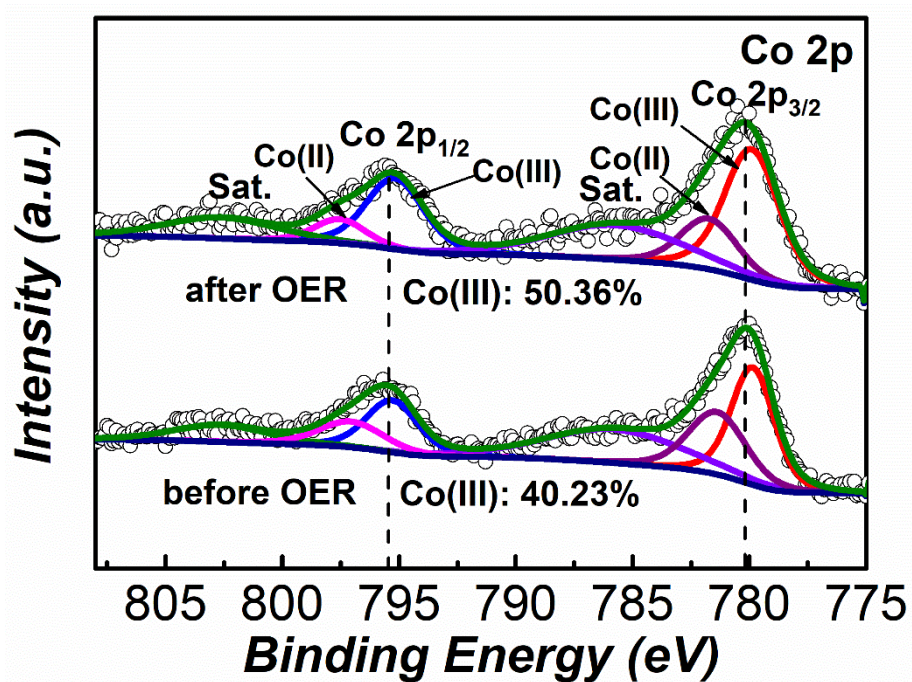


**Figure S20.** Co 2p XPS spectra of Co-Mn- $\alpha$ -Fe<sub>2</sub>O<sub>3</sub> before and after stability test.

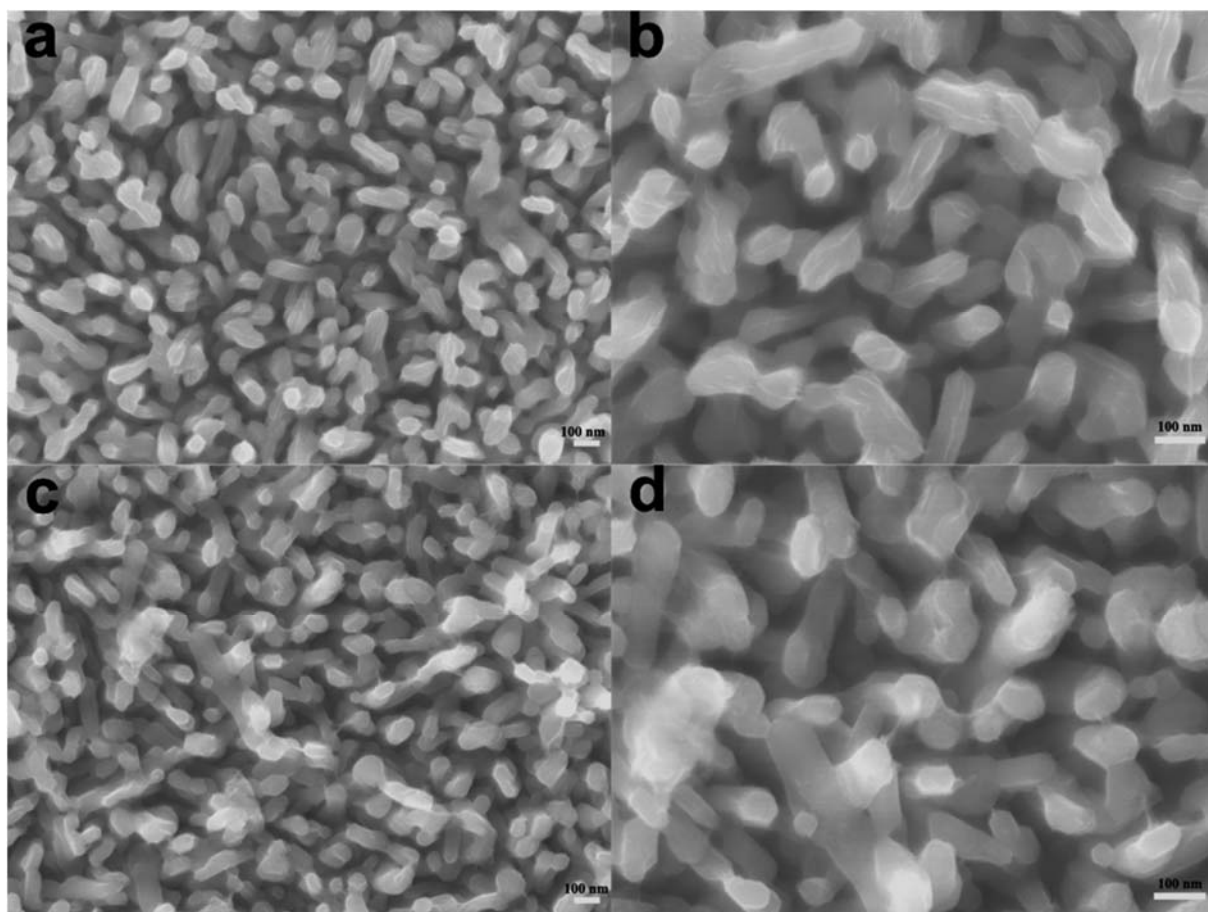


**Figure S21.** SEM images of (a, b) Ni-Mn- $\alpha$ -Fe<sub>2</sub>O<sub>3</sub> and (c, d) Fe-Mn- $\alpha$ -Fe<sub>2</sub>O<sub>3</sub> films.

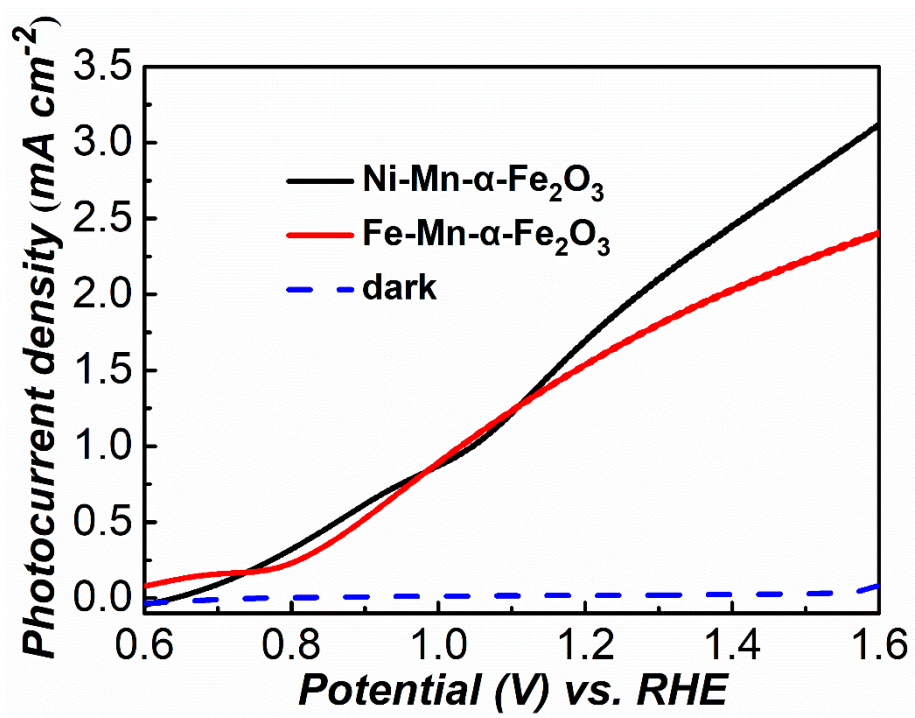


**Figure S22.** J–V curves of Ni-Mn- $\alpha$ -Fe<sub>2</sub>O<sub>3</sub> and Fe-Mn- $\alpha$ -Fe<sub>2</sub>O<sub>3</sub> films.

**Table S1.**  $E_{fb}$  values and carrier densities obtained from Mott-Schottky plots for pristine  $\alpha$ - $Fe_2O_3$ , Mn- $\alpha$ - $Fe_2O_3$ , Co- $\alpha$ - $Fe_2O_3$  and Co-Mn- $\alpha$ - $Fe_2O_3$  photoanodes.

Photoanodes	$E_{fb}$ (V) vs. RHE	Carrier Density ( $cm^{-3}$ )
$\alpha$ - $Fe_2O_3$	0.55	$1.34 \times 10^{20}$
Mn- $\alpha$ - $Fe_2O_3$	0.51	$2.01 \times 10^{20}$
Co- $\alpha$ - $Fe_2O_3$	0.48	$3.40 \times 10^{20}$
Co-Mn- $\alpha$ - $Fe_2O_3$	0.46	$5.41 \times 10^{20}$

**Table S2.** EIS results of different photoanodes calculated by the equivalent circuit model.

Photoanodes	$R_s$ ( $\Omega$ )	$R_{\text{bulk}}$ ( $\Omega$ )	$R_{\text{ct}}$ ( $\Omega$ )
$\alpha$ -Fe <sub>2</sub> O <sub>3</sub>	49.78	103.7	564.9
Mn- $\alpha$ -Fe <sub>2</sub> O <sub>3</sub>	49.91	60.77	414.9
Co- $\alpha$ -Fe <sub>2</sub> O <sub>3</sub>	47.87	38.41	323.2
Co-Mn- $\alpha$ -Fe <sub>2</sub> O <sub>3</sub>	41.39	28.19	299.7

**Table S3.** Comparison of our photoanode to other  $\alpha$ -Fe<sub>2</sub>O<sub>3</sub>-based photoanodes in recent years.

Photoanodes	Onset Potential (V) vs. RHE	Current Density at 1.23 V vs. RHE (mA cm <sup>-2</sup> )	Stability	IPCE Value (%)	References
NiO-P- $\alpha$ -Fe <sub>2</sub> O <sub>3</sub>	0.69	2.08	~ 5% decay after 10 h	38.6 at 1.23V (350 nm)	S1
Zr- $\alpha$ -Fe <sub>2</sub> O <sub>3</sub> NT	~ 0.89	1.50	No decay after 5 h	25.7 at 1.23V (370 nm)	S2
Rh-F-Fe <sub>2</sub> TiO <sub>5</sub> / $\alpha$ -Fe <sub>2</sub> O <sub>3</sub>	0.63	2.12	N.A.	37 at 1.25V (370 nm)	S3
carbon coated $\alpha$ -Fe <sub>2</sub> O <sub>3</sub>	0.77	2.00	N.A.	N.A.	S4
Co-Pi- $\alpha$ -Fe <sub>2</sub> O <sub>3</sub>	~ 0.8	1.28	N.A.	N.A.	S5
IrO <sub>2</sub> /RuO <sub>2</sub> - $\alpha$ -Fe <sub>2</sub> O <sub>3</sub>	0.48	1.52	No decay after 72 h	54 at 1.25V (330 nm)	S6
$\alpha$ -Fe <sub>2</sub> O <sub>3</sub> /FeOOH/Au	0.6	3.2	N.A.	80 at 1.23 V (390 nm)	S7
Co/E-I-Sn- $\alpha$ -Fe <sub>2</sub> O <sub>3</sub>	~ 0.6	2.2	~ 4% decay after 10 h	27 at 1.23V (330 nm)	S8
Au-embedded $\alpha$ -Fe <sub>2</sub> O <sub>3</sub>	0.8	1.025	No decay after 1.5 h	16 at 1.23V (410 nm)	S9
P: $\alpha$ -Fe <sub>2</sub> O <sub>3</sub> /CoPi	0.58	2.0	11% decay after 5 h	28 at 1.23V (360 nm)	S10
$\alpha$ -Fe <sub>2</sub> O <sub>3</sub> /CoAl LDH	0.58	2.0	No decay after 2 h	N.A.	S11
$\alpha$ -Fe <sub>2</sub> O <sub>3</sub> /FeOOH	~ 0.8	0.85	4.4% decay after 70 h	20.2 at 1.23 V (400 nm)	S12
$\alpha$ -Fe <sub>2</sub> O <sub>3</sub> /FeOOH	0.65	1.21	~ 3% decay after 2.5 h	N.A.	S13
<b>Co-Mn-<math>\alpha</math>-Fe<sub>2</sub>O<sub>3</sub></b>	<b>0.6</b>	<b>2.09</b>	<b>~ 3% decay after 10 h</b>	<b>39.1 at 1.23 V (360 nm)</b>	<b>This work</b>

**Reference:**

- [S1] F. Li, J. Li, J. Zhang, L. Gao, X. Long, Y. Hu, S. Li, J. Jin, J. Ma, *ChemSusChem* **2018**, *11*, 2156.
- [S2] C. Li, A. Li, Z. Luo, J. Zhang, X. Chang, Z. Huang, T. Wang, J. Gong, *Angew. Chem. Int. Ed.* **2017**, *56*, 4150.
- [S3] J. Deng, X. Lv, K. Nie, X. Lv, X. Sun, J. Zhong, *ACS Catal.* **2017**, *7*, 4062.
- [S4] T. H. Wang, C.-C. Chiang, Y.-L. Wu, C. Lin, Y.-J. Cheng, Y.-K. Hsieh, C.-F. Wang, C. Huang, *Appl.Catal. B: Environ.* **2017**, *207*, 1.
- [S5] J. Xiao, H. Huang, Q. Huang, L. Zhao, X. Li, X. Hou, H. Chen, Y. Li, *J. Catal.* **2017**, *350*, 48.
- [S6] P. Dias, L. Andrade, A. Mendes, *Nano Energy* **2017**, *38*, 218.
- [S7] L. Wang, H. Hu, N. T. Nguyen, Y. Zhang, P. Schmuki, Y. Bi, *Nano Energy* **2017**, *35*, 171.
- [S8] M. Li, Y. Yang, Y. Ling, W. Qiu, F. Wang, T. Liu, Y. Song, X. Liu, P. Fang, Y. Tong, *Nano Lett.* **2017**, *17*, 2490.
- [S9] P. S. Shinde, S. Y. Lee, J. Ryu, S. H. Choi, J. S. Jang, *Chem. Commun.* **2017**, *53*, 4278.
- [S10] Z. Luo, C. Li, S. Liu, T. Wang, J. Gong, *Chem. Sci.* **2017**, *8*, 91.
- [S11] R. Chong, B. Wang, C. Su, D. Li, L. Mao, Z. Chang, L. Zhang, *J. Mater. Chem. A* **2017**, *5*, 8583.
- [S12] Q. Yu, X. Meng, T. Wang, P. Li, J. Ye, *Adv. Funct. Mater.* **2015**, *25*, 2686.
- [S13] J. Y. Kim, D. H. Youn, K. Kang, J. S. Lee, *Angew. Chem. Int. Ed.* **2016**, *55*, 10854.